Arabian Journal of Chemistry 16 (2023) 105352

Contents lists available at ScienceDirect

Arabian Journal of Chemistry

journal homepage: www.sciencedirect.com

Original article

Enhanced anti-cancer effects of magnetic targeted pH-sensitive curcumin delivery system based on heterogeneous magnetic α-Fe_2O_3/Fe_3O_4 nanoparticles on gastric cancer SGC-7901 cells

Mingyi Ma [a,1], Zhixiang Lv [b,1], You Li [a], Ziye Zhu [a], Chen Ling [a], Dawei He [c,*], Ruijiang Liu [a,*]

[a] *School of Pharmacy, Jiangsu University, Zhenjiang 212013, PR China*
[b] *The People's Hospital of Danyang, Affiliated Danyang Hospital of Nantong University, Zhenjiang 212300, PR China*
[c] *Affiliated Kunshan Hospital, Jiangsu University, Suzhou 215300, PR China*

ARTICLE INFO

Article history:
Received 9 August 2023
Accepted 8 October 2023
Available online 12 October 2023

Keywords:
Heterogeneous magnetic α-Fe_2O_3/Fe_3O_4 nanoparticle
α-Fe_2O_3/Fe_3O_4-CA-CTS-Cur nanosystem
Curcumin

ABSTRACT

Problem: Unhealthy dietary habits and inadequate existing treatment technologies have led to high morbidity and mortality rates in patients with gastric cancer, and the research shows that curcumin has excellent antitumor properties, however, the non-water-soluble characteristic of curcumin limits its applications. To break the limitation, the targeted drug carriers become the urgent need to treat gastric cancer.
Method: The heterogeneous magnetic α-Fe_2O_3/Fe_3O_4 nanoparticles were obtained by rapid combustion method with citric acid (CA) and ferric nitrate as raw materials and anhydrous ethanol as solvent and fuel, and then modified with citric acid (CA) and chitosan (CTS), and loaded curcumin (Cur) to form α-Fe_2O_3/Fe_3O_4-CA-CTS-Cur nanosystem.
Results: The particle sizes of heterogeneous magnetic α-Fe_2O_3/Fe_3O_4 nanoparticles and α-Fe_2O_3/Fe_3O_4-CA-CTS-Cur nanosystem were 24.9 nm and 35.6 nm, respectively, and their respective saturation magnetization were 70.9 emu/g and 30.3 emu/g. The magnetic α-Fe_2O_3/Fe_3O_4-CA-CTS-Cur nanosystem had good stability, excellent drug release rate, and enhanced apoptosis to gastric cancer cells (SGC-7901) through the caspase pathway and ferroptosis of cells.
Conclusions: The magnetic drug delivery nanosystem was successfully constructed, and revealed significant inhibitory and killing effects on SGC-7901 cells, and low toxic and side effects on normal cells.

1. Introduction

Inorganic nanomaterials are vital tools in the toolkit of researchers (Lee et al., 2018; Pei et al., 2023). Based on several years of research, inorganic nanomaterials with unique small-size effects (Nave et al., 2023; Wang et al., 2020), quantum effect (Srivastava et al., 2021; B. Zhang et al., 2023; Zhao et al., 2021), and surface effect have been applied in different fields (De Barros et al., 2021; Feng et al., 2023), including electrochemistry (Foroozandeh et al., 2023; Y.L. Zhang et al., 2023), enzyme immobilization (Ma et al., 2023), energy (Joshi et al., 2022), environmental protection (Zou et al., 2022), and medicine (Da Silva et al., 2023; Lin et al., 2021; P. Wang et al., 2021). Compared with conventional chemotherapeutic drugs, inorganic nanomaterials have prominent advantages in targeted delivery as well as in sustained and controlled release of drugs, and they have excellent biocompatibility and superior loading capacity as drug carriers (Mohamed et al., 2020; Tang et al., 2022; Zhu and Li, 2023). To expand the application of inorganic nanomaterials in the medical field, nanomaterials with controllable preparation, low price, and excellent performance need to be explored and developed.

Gold and silver nanoparticles have attracted great interest due to their unique anti-cancer, antibacterial, and antifungal activities, which can produce ROS (reactive oxygen species) and ATP (inhibition of adenosine triphosphate), thereby causing nucleic acid damage (Shirzadi-Ahodashti et al., 2020; Lan et al., 2023). Gold nanoparticles also have the function of Photothermal therapy and

---

* Corresponding authors.
E-mail addresses: ksdaweihe@163.com (D. He), luckystar_lrj@ujs.edu.cn (R. Liu).
[1] These authors contributed equally to this work.

Peer review under responsibility of King Saud University.

Production and hosting by Elsevier

https://doi.org/10.1016/j.arabjc.2023.105352
1878-5352/

photoacoustic imaging (Zhan et al., 2023), but it is undeniable that the cost of precious metals is relatively expensive, and whether there is retention in the body remains to be studied.

Ferrite is extensively employed in the field of biomedicine due to its affordability, ready availability, and straightforward preparation process. Fe_3O_4 nanoparticles are widely used for magnetic targeting (X. Wang et al., 2023; Ni et al., 2023), drug delivery (Cui et al., 2023; Liu et al., 2023), in vivo image-assisted therapy (Li et al., 2023), magnetic hyperthermia (Khuyen et al., 2023), and tumor detection (Li et al., 2022), for example, Wang et al. conducted a study on the potential anti-cancer properties of Fe_3O_4-NH_2@CS/CuO nanocomplexes and their effects on gastric cancer cell lines. (Y.P. Wang et al., 2021). At the same time as bringing magnetism, aggregation is inevitable, so surface modification methods must be used to reduce aggregation. Fe_2O_3 is also widely used in oncology because of its extremely low magnetic properties. For example, tumor marker detection (Prabhu et al., 2023), photoacoustic imaging (M.Q. Wang et al., 2023; Cao et al., 2022), tumor treatment (Nascimento et al., 2023), etc., especially Fe^{2+} can promote the occurrence of intracellular Fenton reaction and promote the process of iron death (Huang et al., 2023).

Saeed et al. combined Fe_2O_3 and Fe_3O_4 to obtain functionally enhanced nanoparticles (Saeed at al., 2020). To improve the stability of nanoparticles, researchers have proposed more and more methods to prepare heterogeneous α-Fe_2O_3/Fe_3O_4 nanoparticles instead of simple organic cross-linking or coating methods, such as rapid combustion method, sol–gel method, hydrothermal synthesis method, and pulsed AC electrochemical method (Z. Li et al., 2021; Parauha et al., 2021; Peter et al., 2021). Importantly, heterogeneous α-Fe_2O_3/Fe_3O_4 nanoparticles not only combine the advantages of Fe_2O_3 and Fe_3O_4 but also prepare magnetic nanoparticle complexes with target magnetic properties by different preparation methods to overcome the aggregation effect caused by too strong magnetic properties. Heterogeneous magnetic α-Fe_2O_3/Fe_3O_4 nanoparticles, which possess both magnetism and dispersibility, also have good biocompatibility and stability, which are lacking in single magnetite and hematite. They have potential as a carrier in the field of precision therapy (AlSalhi et al., 2020; Mahmoodabadi et al., 2018). In addition, their preparation method is relatively simple; it involves rapid combustion, which is not as demanding on equipment as the hydrothermal method and its preparation cycle takes less time than that of the sol–gel method. Only a calciner is needed to prepare large quantities of heterogeneous magnetic α-Fe_2O_3/Fe_3O_4 nanoparticles in a brief period. Herein, the key parameters of the preparation process are comprehensively discussed. The amount of citric acid, the combustion agent, the calcination temperature, the calcination time, and the heating rate are optimized to obtain heterogeneous magnetic α-Fe_2O_3/Fe_3O_4 nanoparticles with controllable sizes and saturation magnetization.

The successful preparation of ideal inorganic nanocarriers is only the first step; for improved drug delivery, the surface of the nanocarriers needs to be modified to increase drug load. Citric acid and chitosan can improve the dispersibility and biocompatibility of heterogeneous nanoparticles, respectively (Asnani et al., 2020; Bulatao et al., 2023; Jafari et al., 2023; Manna et al., 2023).

Curcumin, a natural plant polyphenol, has therapeutic properties. It not only has anti-inflammatory, antioxidant, antiviral, antitumor, and other pharmacological properties but also has low toxicity and minimal adverse reactions (Kah et al., 2023; S. Li et al., 2021; Li et al., 2017). Furthermore, the carbonyl bond on curcumin can be covalently connected to the amino bond of chitosan by a Schiff base (Yang et al., 2014). The reaction is reversible, and the bond easily breaks in an acidic environment to yield a pH-sensitive magnetic α-Fe_2O_3/Fe_3O_4-CA-CTS-Cur nanosystem.

In the present study, gastric cancer was selected as the research model to explore the mechanism of the magnetic α-Fe_2O_3/Fe_3O_4-CA-CTS-Cur nanosystem vector in SGC-7901 cells at the cellular level. The controlled preparation of heterogeneous magnetic nanoparticles and anticancer effects of dual-targeting intelligent curcumin nanosystem were demonstrated in Scheme 1. Cancer was the focus of scholars' research, but also a major problem that needs to be solved urgently. The investigation of the research could illustrate the basic anticancer effect of drug-loaded nanomaterials and promoted the application of inorganic nanomaterials in biomedicine.

2. Experimental

2.1. Materials

Ferric nitrate nonahydrate ($Fe(NO_3)_3{\cdot}9H_2O$, 98.5 %), citric acid monohydrate ($C_6H_8O_7{\cdot}H_2O$, 99.5 %), anhydrous ethanol (CH_3CH_2OH, 99.7 %), acetic acid (CH_3COOH, 99.5 %), sodium hydroxide (NaOH, 96 %), curcumin ($C_{21}H_{20}O_6$, 95 %), and chitosan (90 % deacetylation) were purchased from Sinopharm Chemical Reagent Co. Ltd. Chitosan was a biochemical reagent, while the other materials were analytical reagents.

Dulbecco's modified Eagle's medium (DMEM) was obtained from HyClone™. Fetal bovine serum (FBS) and a prestained protein ladder were purchased from Thermo Fisher Scientific. Trypsin, Tris-Base, and cysteine were obtained from Biosharp. 3-(4,5-dimethyl-2-thiazolyl)-2,5-diphenyltetrazolium bromide (MTT) was purchased from Aladdin. Phenylmethylsulfonyl fluoride and 5 × loading buffer were purchased from Beyotime Biotechnology. RIPA Lysis Buffer and antibodies were obtained from Amresco and Abcam, respectively. Sodium dodecyl sulfate (CP), ammonium persulfate (AR), methanol (AR), and isopropyl alcohol (AR) were purchased from Sinopharm Chemical Reagent Co., Ltd.

2.2. Preparation of heterogeneous magnetic α-Fe_2O_3/Fe_3O_4 nanoparticles

The preparation of heterogeneous magnetic α-Fe_2O_3/Fe_3O_4 nanoparticles could be divided into two stages: combustion and calcination. First, various amounts of citric acid monohydrate (0.5 g, 1.0 g, 1.5 g, 2.0 g, 2.5 g) were respectively dissolved in beakers containing 20 mL of anhydrous ethanol to form uniform citric acid alcohol solutions with concentrations of 25 g/L, 50 g/L, 75 g/L, 100 g/L, and 125 g/L (corresponding to 0.119 M, 0.238 M, 0.357 M, 0.476 M, and 0.595 M, respectively). Next, 10.5 g of ferric nitrate nonahydrate was added to the beakers to form the solutions with the concentration of 525 g/L (equivalent to 1.30 M). To ensure homogeneity, magnetic stirring was conducted for 60 min until the homogeneous solutions were achieved. Subsequently, the precursor reagents were transferred to a crucible and placed in a ventilated place to ignite and burn until the flame naturally exited. After combustion, the resulting intermediate materials were placed in a temperature-controlled furnace and calcined at 400 °C for 2.0 h with a heating rate of 3 °C/min. The resulting products were then characterized to select the most appropriate dosage of citric acid based on the desired properties and performance.

The chosen optimal amount of citric acid and ferric nitrate nonahydrate of 10.5 g were then dissolved in anhydrous ethanol, resulting in various solutions with volumes of 20 mL, 30 mL, 40 mL, 50 mL, and 100 mL to form various solutions with different concentrations of citric acid (75.0 g/L, 50.0 g/L, 37.5 g/L, 30.0 g/L, and 15.0 g/L; e.i. 0.36 M, 0.24 M, 0.18 M, 0.14 M, and 0.07 M) and ferric nitrate (525.0 g/L, 350.0 g/L, 262.5 g/L, 210.0 g/L, and 105.0 g/L; e.i. 1.30 M, 0.87 M, 0.65 M, 0.52 M, and 0.26 M). Through

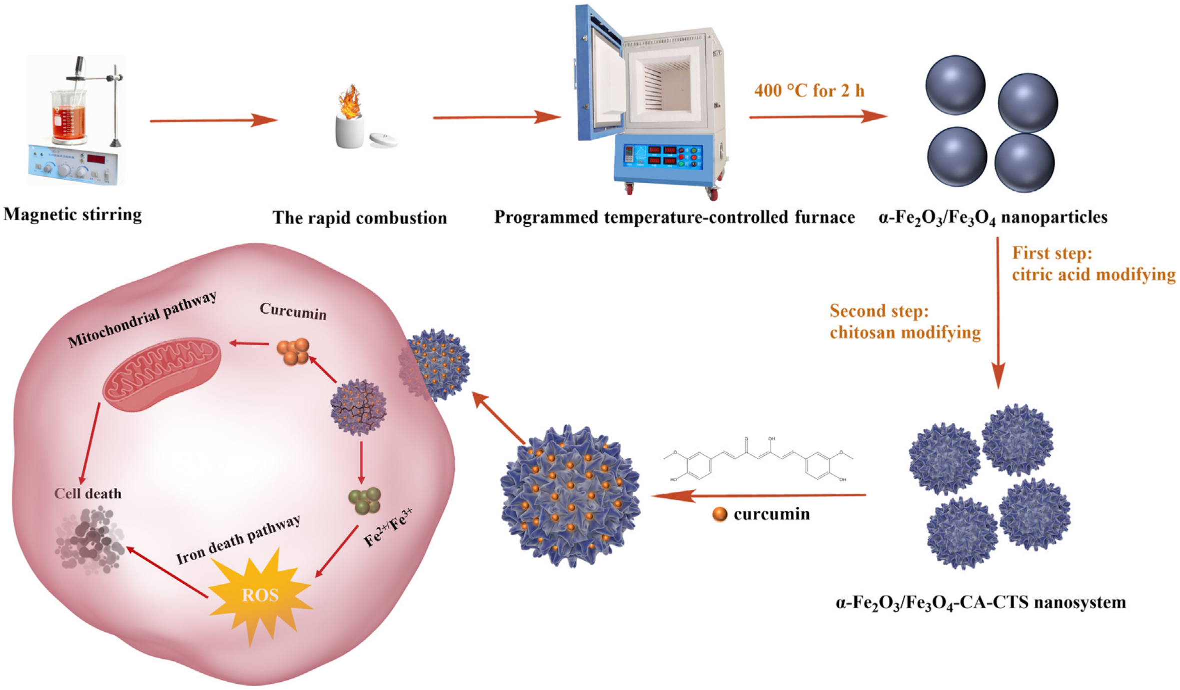

Scheme 1. The preparation process and mechanism diagram of the heterogeneous magnetic α-Fe_2O_3/Fe_3O_4-CA-CTS-Cur nanosystem.

magnetic stirring, a uniform solution was achieved in each case. The ideal amounts of anhydrous ethanol and ferric nitrate nonahydrate were determined based on the outcomes of the previous experimental process.

Based on the previous experimental process and results, the optimal amounts of citric acid, anhydrous ethanol, and ferric nitrate nonahydrate were 1.5 g, 30 mL, and 10.5 g. The ingredits were mixed and formed the homogeneous ethanol solution after magnetic stirring. The precursor was obtained by the rapid combustion. Furthermore, the calcination process should be carried out at a specified temperature and for a specific duration, considering the heating rate. This could be achieved by testing different combinations of the calcination temperature of (150 °C, 200 °C, 250 °C, 300 °C, 350 °C, 400 °C, 450 °C, 500 °C, 600 °C, 700 °C, 800 °C), the calcination time of (0.5 h, 1.0 h, 1.5 h, 2.0 h, 2.5 h), and the heating rate of (1 °C/min, 3 °C/min, 5 °C/min, 7 °C/min, 9 °C/min). These parameters could be adjusted to achieve the desired characteristics of the heterogeneous magnetic α-Fe_2O_3/Fe_3O_4 nanoparticles.

2.3. Synthesis of α-Fe_2O_3/Fe_3O_4-CA nanocomposites

Different concentrations of citric acid solution, namely 0.01 M, 0.03 M, 0.05 M, 0.07 M, and 0.09 M, were prepared. Subsequently, 50.0 mg of the heterogeneous magnetic α-Fe_2O_3/Fe_3O_4 nanoparticles were dispersed in each of the citric acid solutions to form nanomaterial solutions with a consistent concentration of 0.2 mg/mL. These solutions were used for further experiments or analysis. After ultrasonic reaction at 50 °C for 30 min, the residual citric acid was removed by washing and magnetic separation for thrice with double-distilled water. The heterogeneous magnetic α-Fe_2O_3/Fe_3O_4-CA nanocomposites were obtained after drying.

2.4. Construction of α-Fe_2O_3/Fe_3O_4-CA-CTS-Cur nanosystem

Citric acid-coated α-Fe_2O_3/Fe_3O_4 nanoparticles underwent modification with chitosan to enhance their biocompatibility. The process proceeded as follows: various concentrations of chitosan solutions (0.2 mg/mL, 0.4 mg/mL, 0.6 mg/mL, 0.8 mg/mL, 1.0 mg/mL) were prepared by weighing the required quantity of chitosan and dissolving it in a 100 mL acetic acid solution (V/V 1 %) while stirring within a 60 °C water bath. Under ultrasonic conditions, the heterogeneous magnetic α-Fe_2O_3/Fe_3O_4-CA nanocomposites were added to the chitosan solution, and the mixture was incubated for 30 min. Next, a W/V 1 % NaOH solution was added dropwise until the solution became neutral. The reaction system was transferred to a cantilever mechanical stirrer for 3 h to obtain the heterogeneous magnetic α-Fe_2O_3/Fe_3O_4-CA-CTS nanocomposites after the alternate clean by double steaming water and anhydrous ethanol.

Curcumin (20.0 mg) was dissolved in 10 mL of anhydrous ethanol, and the magnetic α-Fe_2O_3/Fe_3O_4-CA-CTS nanocomposites were added to this solution. The mixture was stirred overnight using a cantilever mechanical agitator. Subsequently, the resulting product was alternating washed with anhydrous ethanol and double-distilled water, followed by centrifugation to eliminate any remaining raw materials. Finally, the precipitate was subjected to vacuum-drying, and the heterogeneous magnetic α-Fe_2O_3/Fe_3O_4-CA-CTS-Cur nanosystem was obtained.

2.5. Characterization

The phase composition, the grain size, and structure of the heterogeneous nanomaterials prepared under different conditions were investigated by X-ray diffraction (XRD) (ARL Advant'X, ThermoFisher, USA). The surface morphology and elemental analysis of the nanomaterials before and after modification were obtained using scanning electron microscopy (SEM) (JSM-7800F, JEOL, Tokyo, Japan) and energy dispersive spectroscopy (EDS), respectively. The ultrastructures of the nanomaterials before and after modification were analyzed by transmission electron microscopy (TEM) (JEM-2100(HR), JEOL, Tokyo, Japan). The *in-situ* analysis of the sample, that is, the microscopic correspondence of electron diffraction, was conducted through selected area electron diffraction (SAED) analysis. The magnetic properties and hysteresis loops of the materials were determined using vibrating sample magnetometry (VSM) (7404, Lake Shore, USA). A thermogravimetric analyzer (TGA, STA 449C, NETZSCH Scientific Instruments Trading Ltd., Germany) was employed to measure the relationship between the mass and temperature of the samples under temperature control. Qualitative characterizations of the chemical bond changes for the nanomaterials at different modification stages were performed by Fourier-transform infrared spectroscopy (FTIR) (IS50, Thermo-Fisher, USA). The ultraviolet (UV) absorbancies of the materials before and after drug loading were scanned at full wavelength using a UV–vis spectrophotometer (1600).

2.6. Determination of encapsulation rate and drug load of drug delivery nanosystem

For constructing the drug delivery nanosystem, the supernatant was collected and its volume was measured after the complete reaction of curcumin with the nanocomposites. Absorb a certain amount of supernatant accurately and measure its absorbance at 422 nm. According to the standard curve of curcumin and the ratio of supernatant to the total amount, the amount of unencapsulated curcumin was calculated. The total mass of curcumin used is ‘M’ and the mass of the carrier in the system is ‘m’. The encapsulation rate (EE) and drug load (LC) of the drug delivery nanosystem were calculated according to the following formulas:

$$EE = (M - M_1)/M * 100\% \tag{1}$$

$$LC = (M - M_1)/(m + M - M_1) * 100\% \tag{2}$$

2.7. pH-dependent curcumin release

The drug release behavior of the heterogeneous magnetic α-Fe_2O_3/Fe_3O_4-CA-CTS-Cur nanosystem under different pH conditions was investigated using dialysis. Dialysate (phosphate buffer saline [PBS, pH of 7.4]: anhydrous ethanol = 1:1) at pH values of 1.2, 5.4, 6.8, and 7.4 were prepared. The α-Fe_2O_3/Fe_3O_4-CA-CTS-Cur nanosystem (20 mg) and 2 mL of dialysate were placed in a dialysis bag (MCWO: 2000 Da). The mouth of the bag was sealed and immersed in a conical flask containing 18 mL of dialysis solution. Afterward, the flask was shaken in a thermostatic shock chamber, and dialysis was performed at a speed of 100 rpm at 37 °C. At 1, 2, 3, 4, 5, 6, 7, 8, 9, 10, 24, 36, 48, 60, and 72 h, 3 mL of the release medium was collected, and the same amount of fresh dialysate was returned. The absorbance of the supernatant was measured at 422 nm and the corresponding concentration was calculated according to the standard curve of curcumin. The percentage of curcumin released was calculated according to the following formula:

$$R = \left(20C_n + \sum_{i=1}^{n-1} C_i\right)/\mathrm{m} \times 100\% \tag{3}$$

In the formula, R was the cumulative drug release amount; C_n (μg/mL) was the drug concentration measured at the n^{th} time point; and m (mg) was the final complete drug release amount.

2.8. Cell experiment

2.8.1. MTT assay

In vitro, cytotoxicity test was performed using the MTT assay. MTT was a yellow dye that absorbed light at 490 nm and could be used as a colorimetric measure of cell viability. First, SGC-7901 cells in the logarithmic growth phase were inoculated into 96-well plates at a cell density of 4×10^3 per well. After the cells stably adhered to the dish bottom, they were treated with various concentrations of the test materials for 24 h, 48 h, 72 h, and 96 h, followed by the addition of 10 μL of freshly prepared MTT solution to each well. After incubation for 4 h at 37 ℃ under 5 % CO_2, blue-purple formazan crystals were formed. The supernatant was discarded, and 100 μL DMSO was added into a dissolved formazan. The absorbance of formazan was measured by an enzyme-labeled instrument (iMark, Bio-Rad, USA). Then, as the toxic effects on tumor cells were explored, we also conducted in vitro toxicity studies on normal cells (GES-1) through the above means.

2.8.2. Scratch test

The scratch test was an important means to detect the ability of drugs to inhibit cell migration and invasion. The test was conducted to determine if the prepared drug-loaded nanosystem could inhibit the proliferation and migration of tumor cells. SGC-7901 cells were plated and incubated in six-well plates (1×10^5 cells/well) for 24 h. The cells were streaked with a 1-mL pipette tip, and the culture medium was changed. Subsequently, the 40 μM of α-Fe_2O_3/Fe_3O_4-CA-CTS-Cur nanosystem was exposed to the cells dish. It was important to note that the 40 μM concentration referred to the curcumin content within the α-Fe_2O_3/Fe_3O_4-CA-CTS-Cur nanosystem, and this value was converted to the corresponding weight of α-Fe_2O_3/Fe_3O_4-CA-CTS-Cur nanosystem based on the drug loading rate. After 7 d of continuous administration, the drug was terminated, and the cells were gently washed thrice with fresh PBS. PBS (1 mL) was added to each well and cell migration was observed under an inverted microscope.

2.8.3. Electrochemical detection

SGC-7901 cells at the logarithmic growth stage were uniformly planted in six-well plates at the density of 5 × 10 cells/mL. After being cultured for 24 h, the SGC-7901 cells were treated with 100 μg/mL α-Fe_2O_3/Fe_3O_4, 100 μg/mL α-Fe_2O_3/Fe_3O_4 with magnetic field, 40 μM curcumin, 40 μM α-Fe_2O_3/Fe_3O_4-CA-CTS-Cur with magnetic field, and DMEM. After 24 h of culture, the cells were washed again with PBS and gently digested with trypsin. The cells were prepared into a suspension with 500 μL of PBS (pH 7.4).

The surface of the magnetic glassy carbon electrode (MGCE) was polished with alumina, and the electrode was cleaned twice with ultra-pure water under ultrasonic wave for 30 s each time. Cell suspensions (10 μL) were randomly collected and dropped onto the surface of the MGCE, and the potential changes were detected after drying under a vacuum.

2.8.4. Cell colony formation experiment

SGC-7901 cells at the logarithmic growth stage were uniformly seeded into six-well plates at a cell density of 3×10^3 per well. After the cell adherence was stabilized, the cells were cultured with 100 μg/mL α-Fe_2O_3/Fe_3O_4 nanoparticles with or without magnet, 40 μM α-Fe_2O_3/Fe_3O_4-CA-CTS-Cur with or without magnet, or 40 μM curcumin for 10 d, and fresh drugs were added every 2 d. In the control group, the cells were treated with only DMEM. After terminating the culture, the drugs were fully and gently washed away with fresh PBS, and the cells were fixed with pure methanol for 15 min at 1 mL per well. Next, the cells were stained with fresh Giemsa solution at 500 μL per well for 30 min, and the excess dye was fully removed with flowing double-distilled water. The plates were then photographed under natural light conditions.

2.8.5. Acridine orange-ethidium bromide assay

Acridine orange (AO) was an indicator of ion pump activity. It could penetrate intact cell membranes and bind double-stranded DNA to emit green fluorescence. Ethidium bromide (EB) was a membrane-impermeable DNA probe that bound to DNA and emitted orange fluorescence in damaged cell membranes. So, the AO-EB assay could be employed to detect apoptosis in cells. SGC-7901 cells were seeded at the density of 5 × 10^5 cells/well, and after 24 h culturing when the cells had stably attached to the dish bottom, the cells were treated with 100 μg/mL α-Fe_2O_3/Fe_3O_4 nanoparticles with or without magnet, 40 μM α-Fe_2O_3/Fe_3O_4-CA-CTS-Cur with or without magnet, and 40 μM curcumin. After treatment for 24 h, the medium was removed, and the cells were washed 2–3 times with fresh PBS for gentle washing. Twenty microliters of working solution (AO: EB = 1:1) were added into the cells, and incubated for 5 min at room temperature. Next, the cells were washed 2–3 times with PBS to remove excess dye. Finally, the state of the cells was observed using fluorescence microscopy.

2.8.6. Prussian blue stain

Prussian blue staining test was used to determine if ferrite entered the cells. The Fe ions presented in ferrite, which could be separated by the addition of dilute hydrochloric acid, could react with potassium ferrocyanide to form an insoluble blue compound. If cells engulfed the prepared drug-loaded nanosystem, a stable blue compound would be present in the interstitium of cells, which could be observed under an inverted microscope. SGC-7901 cells were seeded into the six-well plates at the density of 5 × 10^4 cells per well, then the drugs were administered after the cells were stably attached to the dish bottom. After culturing for 24 h, the medium was removed and fresh PBS was added several times for gentle washing to ensure that the extracellular drugs were completely removed. Next, 500 μL of 4 % paraformaldehyde was added to each well, followed by fixing for 15 min. The samples were rinsed twice with tap water and distilled water for 2 min each time. Freshly prepared Perls stain (1 mL) was added to each well, followed by soaking for 20 min. The stain solution was discarded, and the cells were rinsed with distilled water for 3 min. The nuclear fast red staining solution was added, the nuclei were stained for 8 min, and rinsed with distilled water for 30 s. Finally, the cells were observed and photographed with an inverted microscope.

2.8.7. Reactive oxygen species test

A 2,7-dichlorodihydrofluorescein diacetate (DCFH-DA) fluorescent probe was used to determine the level of reactive oxygen species (ROS) through fluorescence microscopy and flow cytometry. SGC-7901 cells (1 × 10^6 cells/well) were inoculated into the six-well plates, followed by incubation overnight. Next, the cells were cultured with 100 μg/mL α-Fe_2O_3/Fe_3O_4 nanoparticles with or without a magnet, 40 μM α-Fe_2O_3/Fe_3O_4-CA-CTS-Cur with or without a magnet, or 40 μM curcumin for 24 h. The DCFH-DA probe was diluted at the ratio of 1:1000 to a working concentration of 10 μmol/L, and 1 mL of the probe was added to each well. The probe was incubated with SGC-7901 cells at 37 °C for 20 min. Subsequently, the cells were counterstained with Hoechst 33,342 for 15 min and then washed to remove the residual probe. Fluorescence microscopy was used for observation and photography. For flow cytometry, the cells were digested with trypsin and collected for quantitative detection.

2.8.8. Malondialdehyde test

Malondialdehyde (MDA) determination was widely performed to assess the level of lipid oxidation. The cells were placed into six-well plates (1 × 10^6 cells per well) and treated with 100 μg/mL α-Fe_2O_3/Fe_3O_4 nanoparticles, 40 μM α-Fe_2O_3/Fe_3O_4-CA-CTS-Cur with N-acetyl cysteine (NAC, 5 mM) and magnet, 40 μM Cur, or 40 μM α-Fe_2O_3/Fe_3O_4-CA-CTS-Cur with or without a magnet after the cells stably attached to the dish bottom. After treatment for 24 h, the medium was removed, and fresh PBS was added for gentle washing. Next, the digested cells were collected after the addition of trypsin. SGC-7901 cells obtained by centrifugation were lysed and the supernatant was collected. 200 μL MDA detection solution was thoroughly mixed with the supernatant, and the mixture was heated for 30 min in a 100 °C water bath. After cooling and centrifugation, the absorbance of each sample was measured at 532 nm (A_{532}) and 600 nm (A_{600}) using an enzyme-labeled instrument.

2.8.9. Superoxide dismutase test

Superoxide dismutase (SOD) activity was detected using the WST-8 method. SGC-7901 cells were seeded in six-well plates at the density of 1 × 10^6 cells/well and cultured overnight at 37 °C with 5 % CO_2. After cultured 24 h with 100 μg/mL α-Fe_2O_3/Fe_3O_4 nanoparticles, 40 μM α-Fe_2O_3/Fe_3O_4-CA-CTS-Cur with NAC (5 mM) and magnet, 40 μM curcumin, or 40 μM α-Fe_2O_3/Fe_3O_4-CA-CTS-Cur with or without magnet, the cells were washed twice with 4 ℃ pre-cooled PBS. The cells were fully lysed by adding SOD sample preparation solution, and the lysate was centrifuged at 12000 rpm for 5 min at 4 °C. The supernatant was collected, and after the sample and control wells were set up, SOD working solution was added to the samples, and cultured at 37 °C for 30 min. The absorbance of the samples at 450 nm was measured on an enzyme-labeled instrument.

2.8.10. Glutathione peroxidase test

Glutathione peroxidase (GSH-Px) catalyzed the decomposition of hydrogen peroxide and protected the structure and functional integrity of the cell membrane (Gao et al., 2022). SGC-7901 cells were seeded into six-well plates at the density of 1 × 10^6 cells/well. After the cells stably adhered onto the dish bottom, they were treated with 100 μg/mL α-Fe_2O_3/Fe_3O_4 nanoparticles, 40 μM α-Fe_2O_3/Fe_3O_4-CA-CTS-Cur with NAC (5 mM), and magnet, 40 μM curcumin, or 40 μM α-Fe_2O_3/Fe_3O_4-CA-CTS-Cur with or without a magnet. After 24 h cultured, the cells were washed twice with pre-cooled PBS at 4 °C. The cells were digested with trypsin, followed by centrifugation and fragmentation. Next, the supernatant was collected and the GSH-Px working solution was added to the sample. The absorbance of the mixture was measured at 412 nm using an enzyme-labeled instrument.

2.8.11. Lactic dehydrogenase test

Cells at the rapid growth stage were seeded into a six-well plate at the cell density of 1 × 10^6 cells/well. After the cells stably adhered onto the dish bottom for 24 h, they were treated with 100 μg/mL α-Fe_2O_3/Fe_3O_4 nanoparticles, 40 μM α-Fe_2O_3/Fe_3O_4-CA-CTS-Cur with NAC (5 mM) and magnet, 40 μM curcumin, or 40 μM α-Fe_2O_3/Fe_3O_4-CA-CTS-Cur with or without magnetic action. After 24 h, the cells were removed from the incubator, placed on ice to remove the medium, and washed twice with pre-cooled PBS at 4 °C. The cells were collected by centrifugation after trypsin digestion. Next, the extraction solution was added to lyse the cells, followed by the addition of the detection solution. Finally, the absorbance of the sample was measured with an enzyme-labeled instrument.

2.8.12. Western blotting

SGC-7901 cells at the density of 1 × 10^6 cells/well were seeded into six-well plates, and the cells adhered stably to the plates overnight. Next, the cells were treated for 24 h with the various test materials, followed by washing twice or thrice with ice-cold PBS, and then the lysis buffer was added to lyse the cells. The cells were scraped with a cell scraper, centrifuged at 12000 rpm at 4 °C for 15 min, and the supernatant was collected. Protein concentration was determined by the bicinchoninic acid assay and gel electrophoresis was carried out using 30 μg of total protein. The polyvinylidene fluoride membrane, which had been successfully loaded with the protein, was incubated overnight at 4 °C with the pre-prepared primary antibody. To prepare the primary antibody, it was diluted 500 times with TBST diluent, and the PVDF membrane was precisely immersed using a 200 μL pipette. Following that, the cells were cultured with the corresponding secondary antibody. The secondary antibody was diluted 1000 times with TBST diluent, and the PVDF membrane was again immersed precisely using a 200 μL pipette. This incubation with the secondary antibody lasted for 2.0 h before proceeding to exposure detection.

2.8.13. Flow cytometry

SGC-7901 cells (5×10^5 cells/well) were cultured in the six-well plates, and after the cells stably attached to the dish bottom, they were treated with blank, 100 μg/mL α-Fe_2O_3/Fe_3O_4 nanoparticles, 40 μM curcumin, or 40 μM α-Fe_2O_3/Fe_3O_4-CA-CTS-Cur with a magnet. After treatment of 24 h, the cells were washed twice or thrice with PBS and digested with trypsin without EDTA. The cells were collected and centrifuged at 8000 rpm for 5 min and resuspended in 100 μL of diluted 1X Annexin V Binding Buffer. Annexin V-FITC (2.5 μL) and propidium iodide (PI, 2.5 μL) were added into the cell suspension, and after gentle mixing, the cells were cultured for 18 min at room temperature. Next, 400 μL of diluted 1X Annexin V binding buffer was added, and the apoptosis of the cells was determined by a flow cytometer.

3. Results and discussion

3.1. Controllable preparation of heterogeneous magnetic α-Fe_2O_3/Fe_3O_4 nanoparticles

Fig. 1 illustrated the TEM image, SAED, and SEM morphology, EDS spectra, XRD pattern, and hysteresis loops of the heterogeneous magnetic α-Fe_2O_3/Fe_3O_4 nanoparticles prepared at the calcination temperature of 400 °C for 2.0 h with the heating rate of 3 °C/min, 1.5 g citric acid, and 30 mL anhydrous. As shown in Fig. 1A, the morphology of the nanomaterials was spherical, and the average particle size was approximately 24.9 nm. As shown in Fig. 1B, the nanoparticles were polycrystalline materials with corresponding crystal surfaces, which was consistent with the XRD results. Fig. 1C showed the SEM image of the heterogeneous nanoparticles, from which the particle structure could be observed. The particle distribution was relatively uniform with an average particle size of 24.9 nm, which was consistent with the TEM results. Therefore, the obtained sample was quite ideal. The EDS spectrum of the nanoparticles (Fig. 1D) showed that the proportion of oxygen and Fe atoms was 58.43 % and 41.47 %, respectively. The Fe/O ratio of single magnetite and hematite was 0.75 and 0.67, respectively, while the element ratio of the prepared nanoparticles was 0.71, which happened to be between the two values, indicating that the prepared nanoparticles was a heterogeneous α-Fe_2O_3/Fe_3O_4 nanoparticles. Fig. 1E showed the XRD pattern of heterogeneous magnetic α-Fe_2O_3/Fe_3O_4 nanoparticles, the Fe_3O_4 standard PDF card (JCPDS No. 99–0073) and α-Fe_2O_3 standard PDF card (JCPDS No. 33–0664). As could be seen from Fig. 1E, most of the sample diffraction peaks corresponded to those of the standard PDF card of α-Fe_2O_3. The characteristic peaks of Fe_3O_4 at diffraction angles of 30° and 43° indicated the existence of Fe_3O_4. In addition, the diffraction peak ratios at 33° and 64° were significantly lower than those in the α-Fe_2O_3 standard PDF card, and there was a Fe_3O_4 diffraction peak at 35.6°, further confirming the presence of Fe_3O_4. This indicated that the proposed heterogeneous α-Fe_2O_3/Fe_3O_4 nanoparticles were successfully prepared. To determine the magnetic properties of the nanoparticles, a vibrating sample magnetometer was employed to detect the hysteresis loops. As depicted in Fig. 1F, the nanoparticles exhibited nearly no remanence and coercivity, signifying its superparamagnetic nature. The saturation magnetization of the nanoparticles was measured at 70.9 emu/g, indicating superior magnetic properties and the potential for achieving magnetic targeting (Hong et al., 2018; Dafeh et al., 2019). However, it was worth noting that the saturation magnetization of pure Fe_3O_4 was 90 emu/g. Notably, in the heterogeneous α-Fe_2O_3/Fe_3O_4 nanoparticles, the saturation magnetization was reduced. This reduction could be attributed to the presence of Fe_2O_3 in the heterogeneous system, as its saturation magnetization was only approximately 0.8 emu/g (Suman et al., 2021). Therefore, the decrease in saturation magnetization in the heterogeneous α-Fe_2O_3/Fe_3O_4 nanoparticles could be due to the presence of the Fe_2O_3 phase.

Fig. 2, Fig. 3, and Table 1 illustrated the XRD patterns and hysteresis loops of heterogeneous α-Fe_2O_3/Fe_3O_4 nanoparticles under different reaction conditions. Fig. 2A and 3A showed the effects of the different amounts of citric acid on heterogeneous α-Fe_2O_3/Fe_3O_4 nanoparticles. The wide and low XRD peaks indicated that the sample had a small crystal grain size. As shown in Fig. 2A, the smallest crystal grain size was observed when the amount of citric acid was about 1.5 g. The relative content of each phase could be roughly obtained from the intensity of the characteristic peaks in the XRD pattern. When the amounts of citric acid were 1.5 g and 2.0 g, the ratios of peaks at 33° and 35.6° were low, indicating that the contents of the Fe_3O_4 phase were high. A high Fe_3O_4 phase ratio corresponded to a stronger saturation magnetization, which was consistent with the hysteresis loops diagram. As shown in Fig. 3A, the saturation magnetization of nanoparticles prepared with 1.5 g and 2.0 g citric acid was relatively high. This was possible because citric acid formed a complex with iron ions, which promoted dispersion, and it also provided more carbon sources for reduction.

The amount of solvent affected the degree of sintering and dispersion. As shown in Fig. 2B and 3B, when the amount of anhydrous ethanol was low, the solute dispersity was low, resulting in a large grain size and low saturation magnetization. However, an excessive amount of anhydrous ethanol increased the degree of sintering during the combustion process and was not conducive to the formation of nanoparticles. Therefore, 30 mL of anhydrous ethanol was selected for subsequent experiments.

Temperature markedly affected the magnetic properties of heterogeneous α-Fe_2O_3/Fe_3O_4 nanoparticles. Twelve temperature points were assessed in this research. As depicted in Fig. 2C and 2D, when the calcination temperature fell within the range of 150–400 °C, there was only a slight alteration in grain size, and all nanoparticles' grain sizes, calculated using Scherrer's equation (Mandal and Samanta, 2021), remained below 16 nm. Additionally, Fig. 3C demonstrated minimal variations in the magnetic properties of the samples within this temperature range. Beyond 400 °C, there was a sharp increase in the grain size of the nanoparticles. Concurrently, the saturation magnetization, as shown in Fig. 3D, rapidly decreased several-fold. This phenomenon could be attributed to the elevated temperature, leading to extensive sintering and oxidation of the samples. However, it's noteworthy that there was a transformation in magnetism within the 400–450 °C range. Analysis of the XRD pattern revealed a reduction in the Fe_3O_4 phase, while the saturation magnetization of Fe_2O_3 was notably low. At this point, Fe_2O_3 became the dominant component within the heterogeneous α-Fe_2O_3/Fe_3O_4 nanoparticles, resulting in significantly diminished saturation magnetization. At 350 °C, the magnetic energy reached its peak, seemingly suggesting optimal calcination conditions. However, upon closer examination using XRD, it became evident that the Fe_2O_3 phase content within the heterogeneous structure was quite low at this temperature. This did not align with the desired heterogeneous structure. To achieve full calcination of the nanoparticles while maintaining a

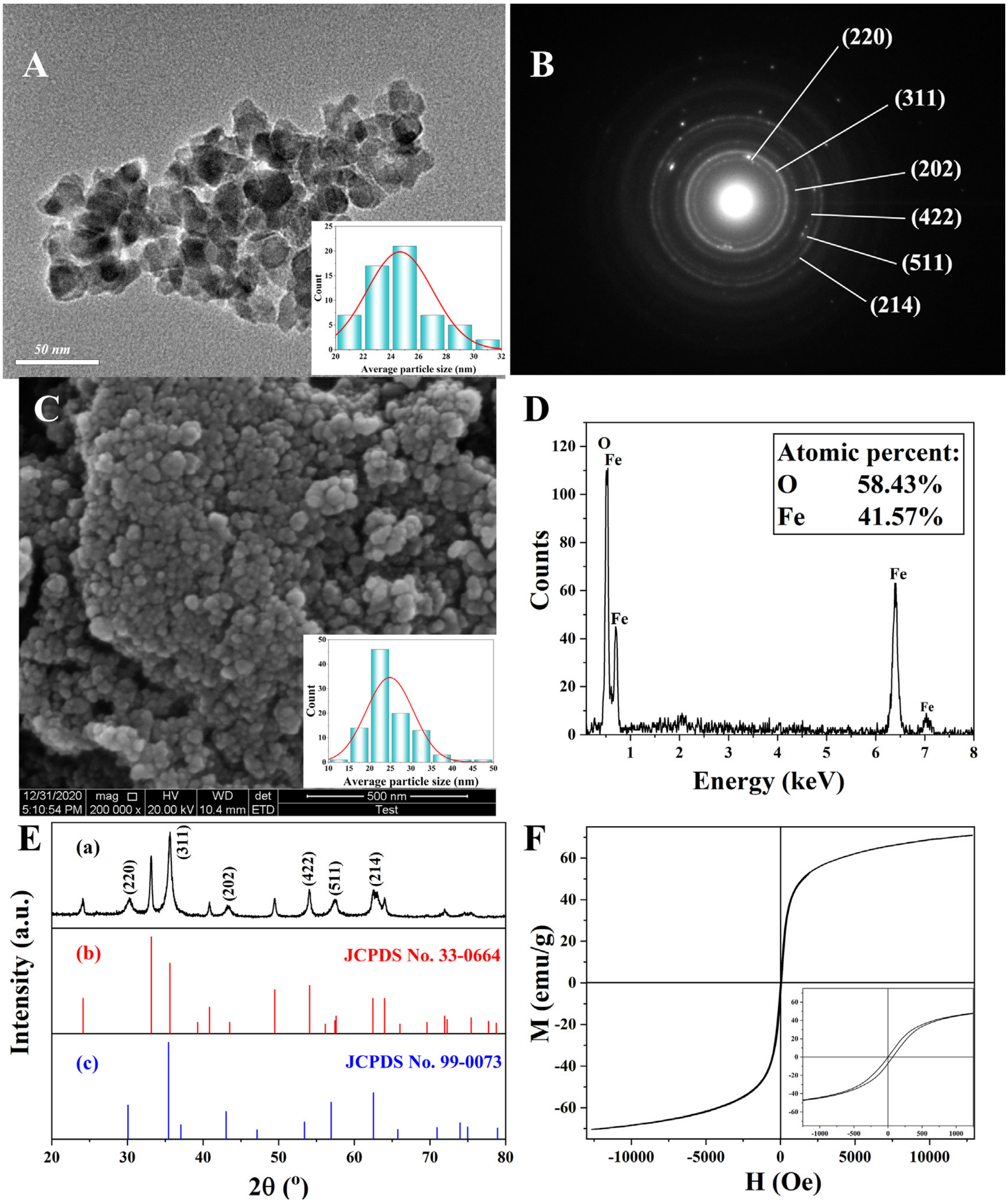

Fig. 1. Transmission electron microscopy (TEM) image (A), selected area electron diffraction (SAED) spectrum (B), scanning electron microscopy (SEM) image (C), energy dispersive spectroscopy (EDS) image (D), X-ray diffraction (XRD) pattern of the magnetic α-Fe_2O_3/Fe_3O_4 nanoparticles (a), the Fe_3O_4 standard PDF card (b) and α-Fe_2O_3 standard PDF card (c) (E), and vibrating sample magnetometry (VSM) curve (F) of the heterogeneous magnetic α-Fe_2O_3/Fe_3O_4 nanoparticles, which was prepared at the best condition: 1.5 g citric acid, 30 mL anhydrous ethanol, the calcination temperature of 400 °C, the calcination time of 2.0 h, and the heating rate of 3 °C/min.

smaller grain size, the calcination temperature of 400 °C was selected for subsequent experiments.

To further explore the controllable preparation of the heterogeneous magnetic α-Fe_2O_3/Fe_3O_4 nanoparticles, the experimental conditions such as the calcination time and the heating rate were analyzed. The XRD analysis in Fig. 2E(d) and 2F(b) revealed the presence of the smallest grain size, accompanied by the lowest XRD peak, under the conditions of a 2.0 h calcination time and a heating rate of 3 °C/min. Fig. 3E and 3F showed that the saturation magnetization decreased with the duration of calcination, which was caused by the increasing degree of oxidation. However, the heating rate had little influence on the magnetic properties. Because the calcination time was related to the oxidation and sintering of nanoparticles, a short calcination time was not conducive to the formation of products, while a long calcination time increased the oxidation degree of products. Therefore, 2.0 h was selected as the calcination time. Different heating rates affect the stability of the production process. When different nanoparticles were subjected to the same calcination temperature, the same degree of oxidation was observed for all the nanoparticles. The influence of the heating rate was greater than that of the saturation magnetization on particle size formation. Thus, a heating rate of 3 °C/min was selected based on a thorough consideration of both parameters.

In summary, based on the dynamic particle size measurements under different conditions in Fig. 4 and Table 1, it could be

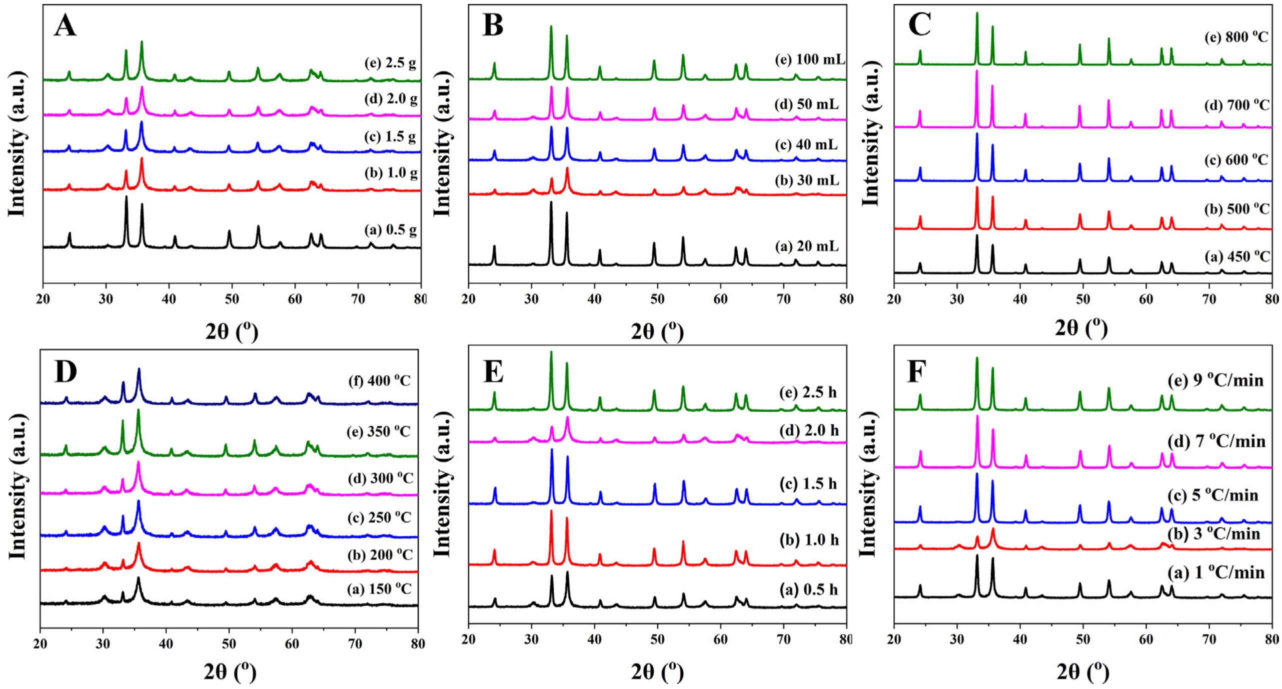

Fig. 2. X-ray diffraction (XRD) patterns of the heterogeneous magnetic α-Fe_2O_3/Fe_3O_4 nanoparticles prepared with various amounts of citric acid (A) and anhydrous ethanol (B) at different calcination temperatures (C and D) for different calcination times (E) with different heating rates (F).

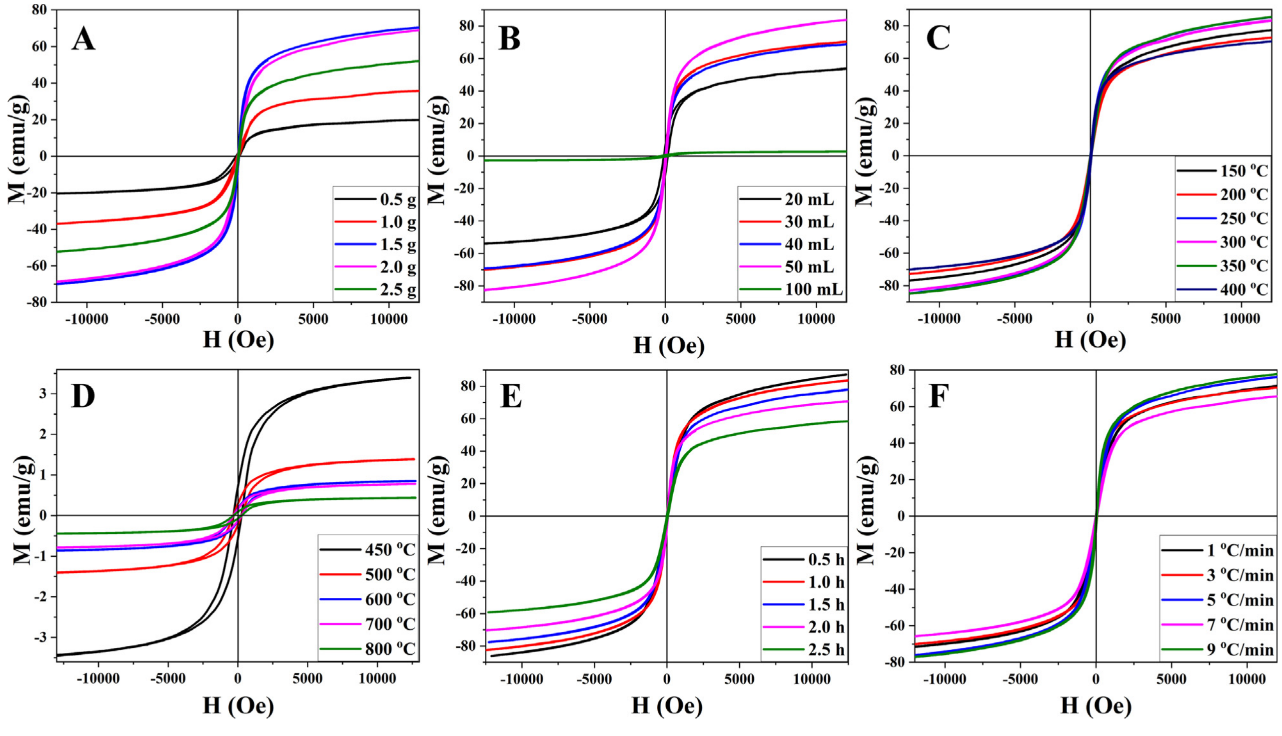

Fig. 3. Hysteresis loops of heterogeneous magnetic α-Fe_2O_3/Fe_3O_4 nanoparticles prepared with various amounts of citric acid (A) and anhydrous ethanol (B) at different calcination temperatures (C and D) for different calcination times (E) with different heating rates (F).

observed that the optimal hydrated particle size was achieved when using 1.0 g of citric acid and 20 mL of anhydrous ethanol. When varying the calcination temperature between 150 and 400 °C, the hydrodynamic size of the nanoparticles displayed an initial phase of nearly constant size, followed by an increase, and finally a decrease. This trend was a result of the combined effects of the magnetic properties and grain size of the nanoparticles. Furthermore, at the calcination temperature of 400 °C, the hydrodynamic size reached its minimum value of 203.1 nm, which was considerably larger than the particle size observed using transmission and scanning techniques. This phenomenon could be attributed to the high surface energy of the nanoparticles, making them prone to aggregation and attraction to one another. Additionally, the strong saturation magnetization property of the prepared

Table 1
Hydrodynamic size and saturation magnetization of nanoparticles with different preparation schemes.

Preparation scheme					Hydrodynamic size (nm)	Saturation magnetization (emu/g)
Citric acid (g)	Anhydrous ethanol (mL)	Calcination temperature (°C)	Calcination time (h)	Heating rate (°C/min)		
0.5	20	400	2	3	114.91	19.82
1.0	20	400	2	3	99.01	35.68
1.5	20	400	2	3	203.14	53.8
2.0	20	400	2	3	142.65	68.90
2.5	20	400	2	3	220.98	51.97
1.5	30	400	2	3	211.66	70.33
1.5	40	400	2	3	289.82	68.88
1.5	50	400	2	3	316.55	83.80
1.5	100	400	2	3	112.29	2.70
1.5	30	150	2	3	327.07	77.19
1.5	30	200	2	3	301.42	72.68
1.5	30	250	2	3	300.29	82.86
1.5	30	300	2	3	441.48	82.92
1.5	30	350	2	3	333.01	85.41
1.5	30	400	2	3	211.66	70.33
1.5	30	450	2	3	41.22	3.39
1.5	30	500	2	3	72.64	1.39
1.5	30	600	2	3	48.09	0.85
1.5	30	700	2	3	13.45	0.78
1.5	30	800	2	3	226.63	0.44
1.5	30	400	0.5	3	–	87.23
1.5	30	400	1	3	–	83.68
1.5	30	400	1.5	3	–	77.95
1.5	30	400	2.5	3	–	58.46
1.5	30	400	2	1	–	71.33
1.5	30	400	2	5	–	76.18
1.5	30	400	2	7	–	65.63
1.5	30	400	2	9	–	77.83

nanoparticles also contributed to their agglomeration. It was worth noting that the particle size measured by the particle size analyzer included the influence of water molecules, leading to an overestimation of the hydrodynamic size. Taking into account the comprehensive SEM, VSM, and DLS results, the optimal preparation conditions were determined as follows: 1.5 g of citric acid, 30 mL of anhydrous ethanol, the calcination temperature of 400 °C, the calcination time of 2.0 h, and the heating rate of 3 °C/min. Under these conditions, the average particle size of the magnetic α-Fe_2O_3/Fe_3O_4 heterogeneous nanoparticles was 24.9 nm, with a saturation magnetization of 70.9 emu/g, indicating superparamagnetic behavior.

3.2. Construction and drug release behavior of magnetic α-Fe_2O_3/Fe_3O_4-CA-CTS-Cur nanosystem

Fig. 5 displayed the SEM, TEM, EDS images, and VSM curves of the heterogeneous magnetic α-Fe_2O_3/Fe_3O_4 nanoparticles modified with citric acid and chitosan and loaded with curcumin (magnetic α-Fe_2O_3/Fe_3O_4-CA-CTS-Cur nanosystem). As shown in Fig. 5A, the modification could not destroy the structure of nanoparticles. Moreover, most of the particle sizes were approximately 35.6 nm, which was slightly higher than that of the naked heterogeneous magnetic nanoparticles, mainly due to the encapsulation of chitosan. These results confirmed that the prepared nano-drug delivery system could be miniaturized and had the potential for application in the biological field. Fig. 5B showed the transmission diagram of the drug-loaded nanosystem. An encased shell composed of citric acid and chitosan, as well as heterogeneous nanoparticle nuclei, could be observed. The average thickness of the shell and the size of the middle core of the prepared nanosystem were 9.5 nm and 25.2 nm, respectively. The EDS map of the α-Fe_2O_3/Fe_3O_4-CA-CTS-Cur nanosystem showed that carbon, iron, and oxygen were detected (Fig. 5C). In addition, the Fe/O ratio decreased significantly, indicating the presence of organic compounds in the drug-loaded nanosystem. This result was consistent with the scanning results, indicating the effective modification of citric acid and chitosan on heterogeneous nanoparticles. Fig. 5D showed the VSM diagram of the drug-loaded nanosystem. Compared with the bare magnetic α-Fe_2O_3/Fe_3O_4 nanoparticles (Fig. 1F), the magnetic properties of the drug-loaded nanosystem with encapsulated shells significantly decreased. The saturation magnetization of the nanosystem was also reduced to 30.3 emu/g. This reduction in magnetic properties was expected because the organic matter had no magnetic properties, and the magnetic properties of drug-loaded nanosystem inevitably decreased when encapsulated by organic matter. Fig. 5E showed the full spectrum analysis of heterogeneous nanoparticle elements, from which it could be seen that the elements contained in the drug-loaded nanosystem were iron, oxygen, and carbon. Iron and oxygen were undoubtedly attributed to heterogeneous magnetic α-Fe_2O_3/Fe_3O_4 nanoparticles. Element carbon should belong to the organic matter of the envelope. Fig. 5 F showed the spectral peak division of Fe2p. Iron was divided into five peaks, which were located at 710.2 eV and 712.1 eV, 717.9 eV, 724.4 eV, and 729.4 eV corresponding to $Fe2p_{3/2}$ in Fe_3O_4, $Fe2p_{3/2}$ in α-Fe_2O_3, Fe_3O_4 in α-Fe_2O_3, and $Fe2p_{3/2}$ in Fe_3O_4, respectively $Fe2p_{1/2}$, $Fe2p_{1/2}$ in α-Fe_2O_3 (Fiore et al., 2022), the appearance of these peaks indicated that the entire encasing process did not change the chemical valence state of the element, and the position of the peak was slightly shifted to a small angle, which might be due to the presence of a large number of carboxyl groups around the iron element. Because citric acid first entered the inclusion system, it contained a large number of carboxyl electron-absorbing groups, resulting in a slight change in the chemical environment around the iron. These results provided evidence for the successful preparation of magnetic α-Fe_2O_3/Fe_3O_4-CA-CTS-Cur nanosystem.

Fig. 6 contained TGA curves, derivative thermogravimetric (DTG) curves, full-wavelength scanning, FTIR images, and the hydrodynamic dimension of the heterogeneous magnetic α-

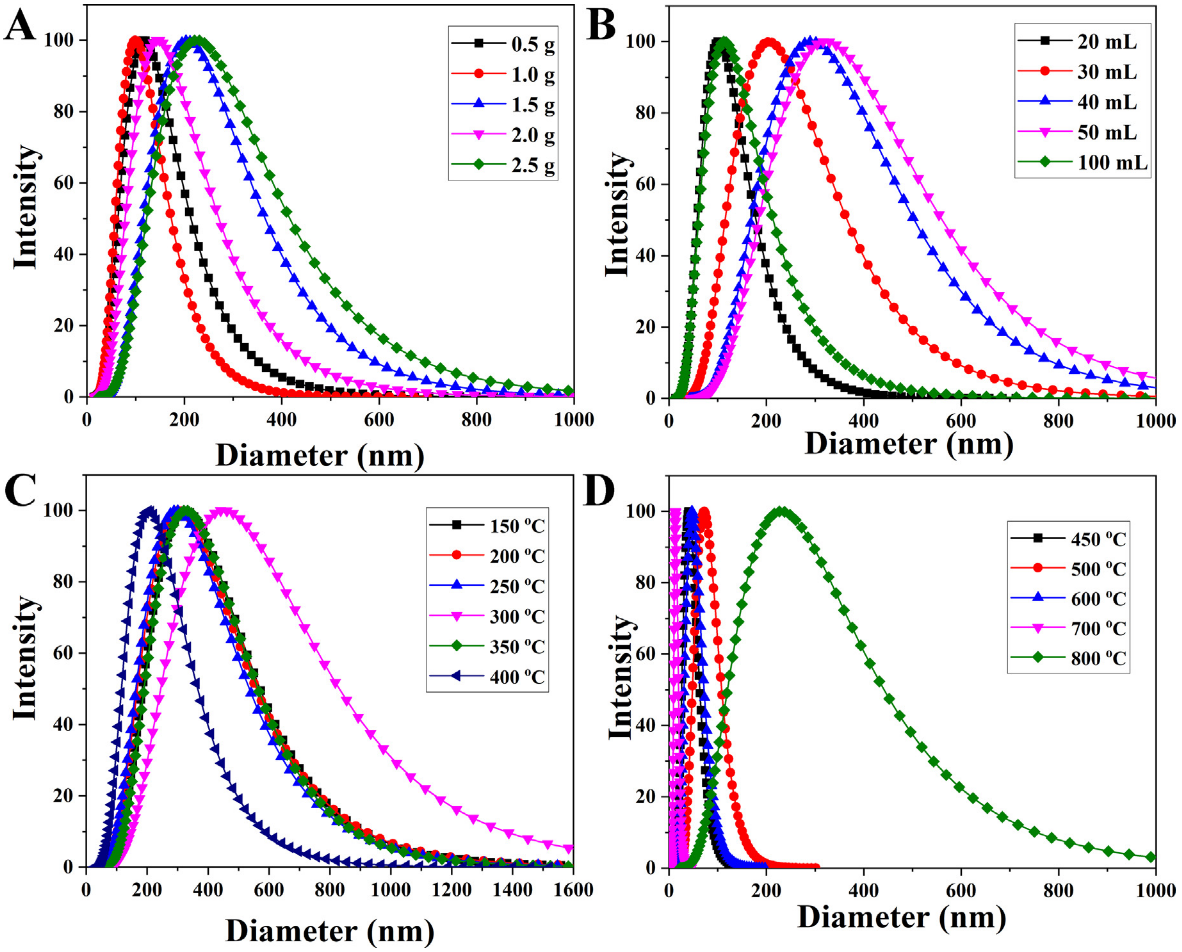

Fig. 4. Hydrodynamic dimensions of the heterogeneous magnetic α-Fe_2O_3/Fe_3O_4 nanoparticles prepared at different proportions of citric acid (A), anhydrous ethanol volume (B), and calcination temperature (C and D).

Fe_2O_3/Fe_3O_4 nanoparticles modified with citric acid and chitosan and loaded with curcumin (magnetic α-Fe_2O_3/Fe_3O_4-CA-CTS-Cur nanosystem). Fig. 6A depicted the TGA curve illustrating the mass changes of the drug-loaded nanosystem as the temperature varied under controlled conditions. This analysis allowed for the determination of the nanocomposites 's thermal stability and composition. The results indicated that the drug-loaded nanosystem exhibited a minor weight loss stage ranging from 29 °C to 137 °C, resulting in a 10.9 % reduction in mass. This decrease was primarily attributed to the evaporation of the nanosystem's water content. Between 224 °C and 572 °C, a significant weight loss of 34.9 % occurred, primarily due to the decomposition of curcumin and citric acid, with the main chain of chitosan also starting to break down at this stage. Additionally, a relatively rapid weight loss of 14.6 % was observed within the temperature range of 572–654 °C, which could be attributed to the complete decomposition of chitosan. Fig. 6B depicted the first differential TGA curve of the drug-loaded nanosystem. The weight loss rate curve of the measured nanosystem concerning temperature was also known as the DTG curve. This curve provided insights into the specific temperature during weightlessness, and the inflection point of the TGA curve indicated the temperature value. This temperature value corresponded to the peak of the DTG curve, representing the maximum rate of weight loss. Therefore, it could be easily seen from Fig. 6B that the weight loss rate of water molecules was the fastest at 72 °C, whereas the fastest decomposition of curcumin and chitosan was observed at 262 °C and 594 °C (Fazeli et al., 2022), respectively, which was consistent with the results in Fig. 6A. Fig. 6C depicted the detection of magnetic α-Fe_2O_3/Fe_3O_4 nanoparticles, curcumin, and drug-loaded nanosystem by a full spectrum scan. There was a chromophore (a benzene ring) on curcumin. Hence, its UV absorption peak could be seen when it was scanned at full wavelength (Fig. 6C). The maximum absorption wavelength of curcumin was 422 nm. The successful loading of curcumin was confirmed by scanning the UV absorption spectra of the three nanomaterials. As shown in the spectrogram of the magnetic α-Fe_2O_3/Fe_3O_4 nanoparticles, there was no UV absorption peak in the visible band. However, the drug-loaded nanosystem had the same UV absorption peak as curcumin in the range of 400–450 nm, with a maximum absorption peak at 422 nm. This indicated that curcumin was present in the drug-loaded nanosystem, which further provided evidence for the successful loading of curcumin. Fig. 6D showed the infrared spectra of magnetic α-Fe_2O_3/Fe_3O_4 nanoparticles, citric acid, curcumin, chitosan, α-Fe_2O_3/Fe_3O_4-CA, α-Fe_2O_3/Fe_3O_4-CA-CTS, and α-Fe_2O_3/Fe_3O_4-CA-CTS-Cur nanosystem. It could be seen from the infrared spectrum of the magnetic α-Fe_2O_3/Fe_3O_4 nanoparticles that only the peaks at 560 cm^{-1} and 455 cm^{-1} belonging to the ferro-oxygen bond exist in the spectrum, and there were no additional miscellaneous peaks. The results illustrated that heterogeneous α-Fe_2O_3/Fe_3O_4 nanoparticles were obtained at the experimental scheme: 1.5 g citric acid, 30 mL anhydrous ethanol, the calcination temperature of 400 °C, the calcination time of 2.0 h, and the heating rate of 3 °C/min. As could be seen from the infrared image of citric acid, the C = O bond on the special car-

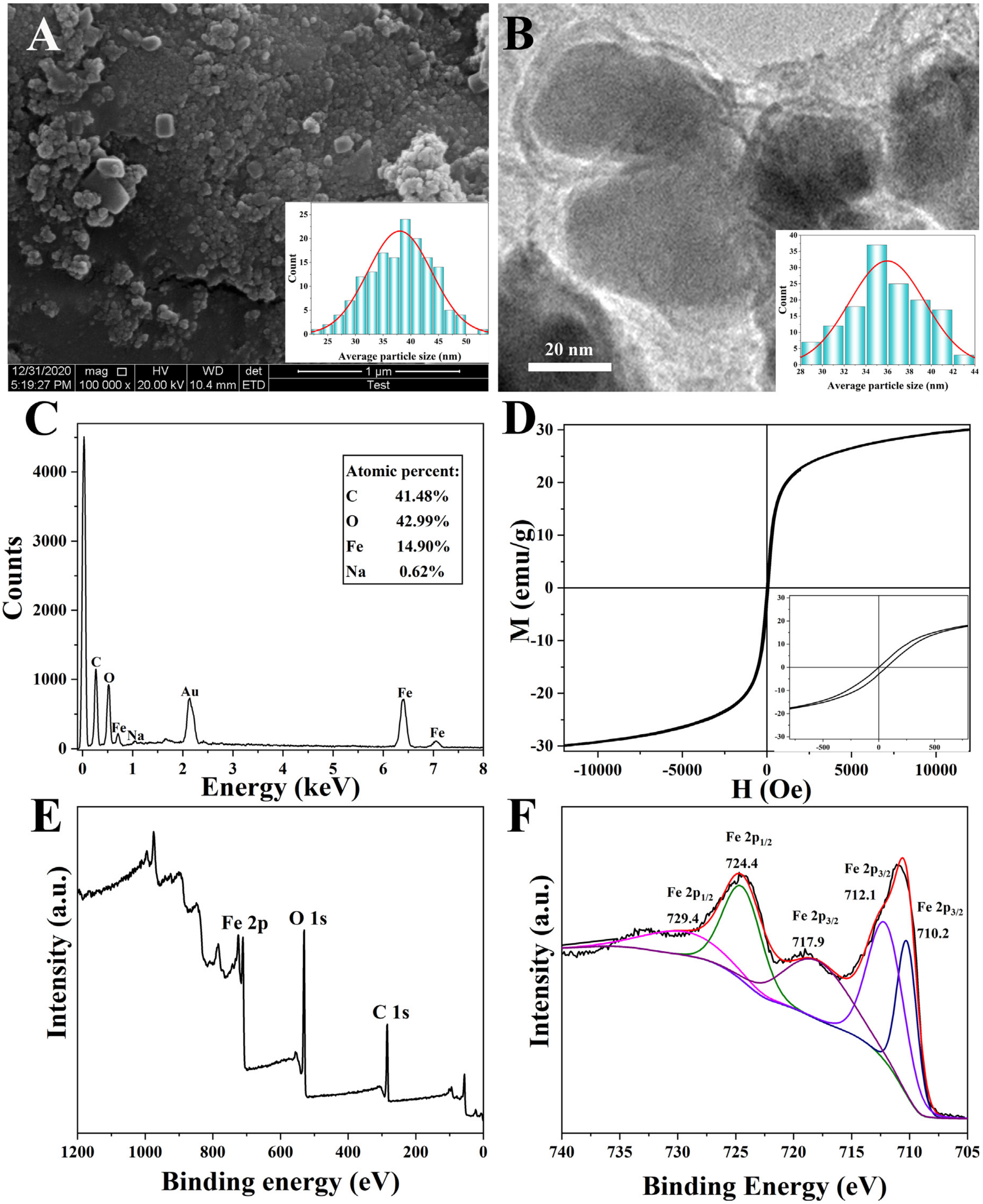

Fig. 5. Scanning electron microscopy (SEM) image (A), transmission electron microscopy (TEM) image (B), energy dispersive spectroscopy (EDS) image (C), vibrating sample magnetometry (VSM) curve (D), XPS spectrum of survey scan (E) and deconvolution of Fe 2p (F) of the heterogeneous magnetic α-Fe_2O_3/Fe_3O_4-CA-CTS-Cur nanosystem.

boxyl group of citric acid peaks appeared at 1731 cm^{-1}, and the O–H bond on the carboxyl group peaks appeared at 3295 cm^{-1}. Moreover, the carbonyl peak of α-Fe_2O_3/Fe_3O_4-CA at 1731 cm^{-1} remained, whereas the peak of the O–H bond at 3295 cm^{-1} disappeared. This was because, in the modification process, the H atom was removed after the hydrolysis of citric acid, and the electron-withdrawing group COO– appeared for better modification of the surface of the nanoparticles. The peak of the ferro-oxygen bond indicated that citric acid was successfully modified on the surface of the magnetic α-Fe_2O_3/Fe_3O_4 nanoparticles. According to the infrared spectra of chitosan, the characteristic peaks of the amino group appeared at 3440 cm^{-1} (N–H) and 1090 cm^{-1} (C-N). The absorption of the hydroxyl group in the infrared region also contributed to the wide peak at 3440 cm^{-1}, and the peak at 1640 cm^{-1} could be attributed to the water. Notably, in the FTIR spectrum of α-Fe_2O_3/Fe_3O_4-CA-CTS, the peak at 3440 cm^{-1} disappeared, and the carbonyl peak was slightly redshifted. This phenomenon was likely caused by the reaction between chitosan and citric acid. In the infrared spectrum of curcumin, the peaks of the ether and carbonyl bonds at 1222 cm^{-1} and 1627 cm^{-1} were

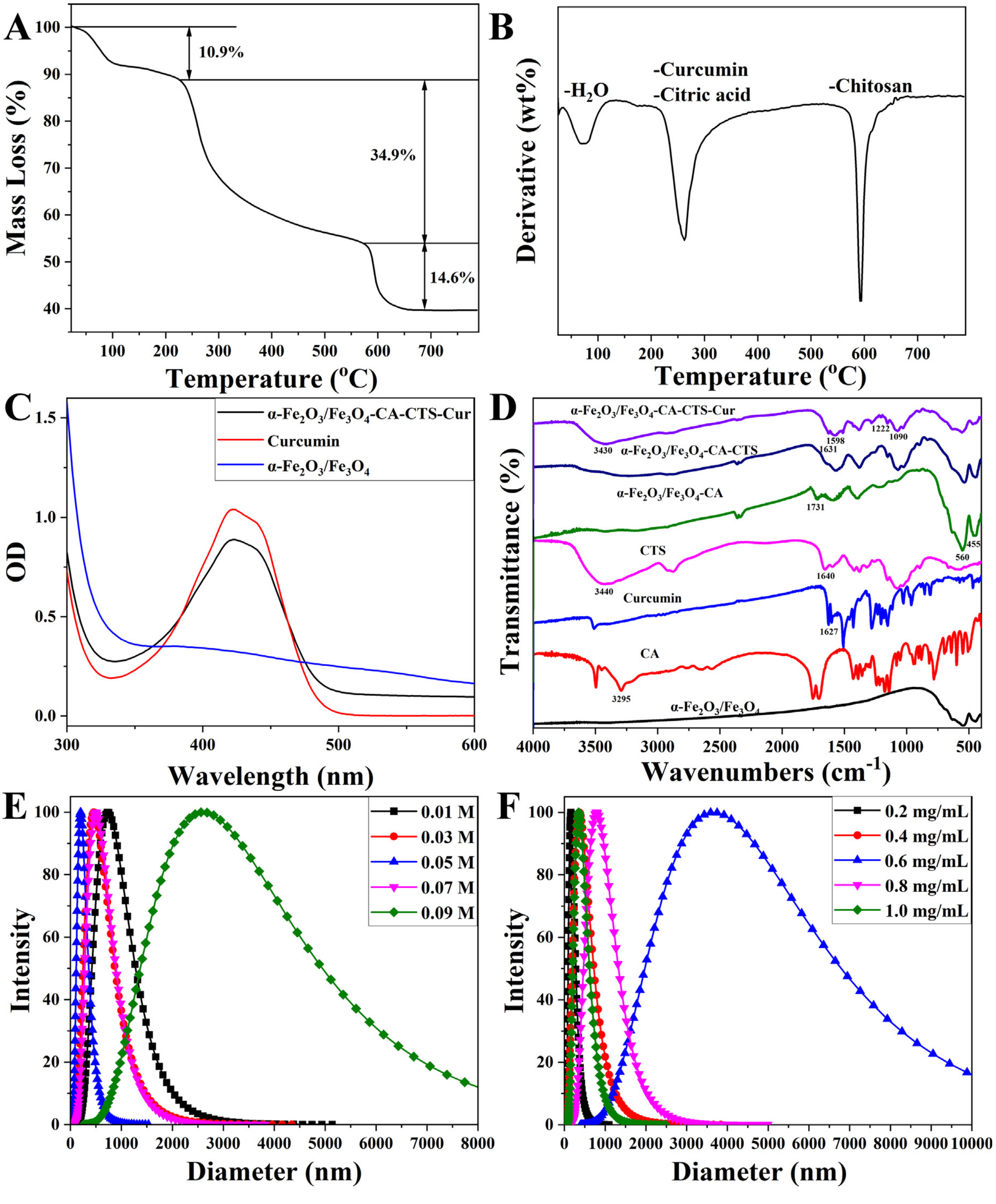

Fig. 6. Thermogravimetric analysis (TGA) image (A), derivative thermogravimetric (DTG) (B), full wavelength scanning patterns of the heterogeneous magnetic α-Fe_2O_3/Fe_3O_4-CA-CTS-Cur nanosystem, curcumin, and the heterogeneous magnetic α-Fe_2O_3/Fe_3O_4 nanoparticles (C), fourier-transform infrared spectroscopy (FTIR) spectra of the heterogeneous magnetic α-Fe_2O_3/Fe_3O_4 nanoparticles, citric acid monohydrate (CA), curcumin (Cur), chitosan (CTS), α-Fe_2O_3/Fe_3O_4-CA, α-Fe_2O_3/Fe_3O_4-CA-CTS, and α-Fe_2O_3/Fe_3O_4-CA-CTS-Cur nanosystem (D), hydrodynamic dimensions of heterogeneous magnetic α-Fe_2O_3/Fe_3O_4 nanoparticles at different proportions of citric acid (E) and chitosan (F).

visible. However, in the infrared spectrum of the α-Fe_2O_3/Fe_3O_4-CA-CTS-Cur nanosystem, the peak of the carbonyl bond changed to the peak of the C = N bond in the Schiff base, and the peak position also changed to 1598 cm^{-1}, but the ether bond peak remained unchanged (Eddarai et al., 2022; Ren et al., 2022; Sornsumdaeng et al., 2021). This result confirmed that the carbonyl group of curcumin and the primary amine group of chitosan could be covalently linked by the Schiff base. The reaction was reversible and could be hydrolyzed under weakly acidic conditions, which facilitated the pH-sensitive release of drugs from the nanosystem. In addition, the infrared image of the final product also showed that the peak at 1090 cm^{-1} was attributed to chitosan, the peaks at 560 cm^{-1} and 455 cm^{-1} were for heterogeneous magnetic α-Fe_2O_3/Fe_3O_4 nanoparticles, and the peak at 3430 cm^{-1} was for water. These results confirmed the successful preparation of the α-Fe_2O_3/Fe_3O_4-CA-CTS-Cur nanosystem. In addition, the hydrodynamic sizes (Fig. 6E and 6F) of the citric acid and chitosan-coated heterogeneous magnetic α-Fe_2O_3/Fe_3O_4 nanoparticles were measured in different proportions, the optimum conditions were investigated. The optimal drug carrier was prepared under the conditions of citric acid 0.05 M and chitosan 0.2 mg/mL. As shown in Table 2, the encapsulation rate and drug-loading rate of the α-Fe_2O_3/Fe_3O_4-CA-CTS-Cur nanosystem were 48.5 % and 9.7 %, respectively.

Fig. 7 described the drug release curves of the drug-loaded nanosystem as measured by dialysis at four different pH values. The released amount of the drug was measured according to the standard curve of curcumin (Fig. S1). As shown in Fig. 7A, at the simulated pH of gastric juice (pH 1.2), the results of the drug release test indicated that curcumin release was slow, and the final equilibrium release was relatively small, which was also reflected in Fig. S2. This was because in a highly acidic environment, curcumin had poor stability and its carbonyl group underwent a nucleophilic reaction, which caused its decomposition. Therefore, once curcumin was released into a strongly acidic solution, it decomposed. Therefore, the least amount of curcumin was detected by UV at pH 1.2 (Fig. 7A). At pH 5.4 (Fig. 7B), the release rate of curcumin increased significantly, which was faster than that at pH 6.8 (Fig. 7C) and 7.4 (Fig. 7D), indicating that the weakly acidic environment was conducive to the release of curcumin from the α-Fe_2O_3/Fe_3O_4-CA-CTS-Cur nanosystem. In addition, as shown in Fig. S2, the final release amount of curcumin in the tumor tissue microenvironment simulation solution at pH 5.4 was larger than that in other pH environments, indicating that the release amount of curcumin in the simulated tumor intracellular matrix (pH 5.4) was greater than those in the tumor extracellular setting (pH 6.8) and normal physiological environment (pH 7.4). This phenomenon confirmed the pH sensitivity of the prepared drug-loaded nanosystem, which was caused by the instability of the covalent bond of the Schiff base linking curcumin to chitosan in a weakly acidic environment, leading to easy hydrolysis for curcumin release. To further investigated the drug release property of the α-Fe_2O_3/Fe_3O_4-CA-CTS-Cur nanosystem, the zero-order kinetic equation of drug release at a constant rate, first-order kinetic equation of drug release at a constant proportion per unit time, and Higuchi kinetic equation of drug release following Fick's law was used to analyze the drug release data. The representative equations were as follows (Bian et al., 2022; Gupta et al., 2023; Nematollahi et al., 2021):

$$M_t = a + bt \tag{4}$$

$$M_t = M * (1 - e^{-k_1 t}) \tag{5}$$

$$M_t = ct^{1/2} + d \tag{6}$$

Where M_t was the cumulative drug release rate at t time, and a and b were the parameters of the zero-order equation. M was the total cumulative release rate and k_1 was the parameter of the first-order equation. c and d were parameters of Higuchi's equation. It could be seen from the fitting results in Table 3 that the correlation coefficient fitting of the first-order kinetic equation to the experimental data exceeded 0.95, and at pH 5.4, the correlation coefficient fitting of the first-order kinetic equation reached 0.99, but the fitting results of other equations to the drug release data at all pH values were lower than 0.85. These results suggested that the simulated curcumin release behavior of the drug-loaded nanosystem was in line with the first-order kinetic equation. This indicated that the prepared drug-loaded nanosystem was a sustained release system. Moreover, the amount of curcumin released was related to the total amount of drug in the body, and the half-life of release was constant.

Figure S3 showed the stability of magnetic α-Fe_2O_3/Fe_3O_4 nanoparticles and magnetic α-Fe_2O_3/ Fe_3O_4-CA-CTS-Cur drug delivery nanosystem in DMEM medium for 10 min, 24 h, and 48 h. It was obvious from the figure that even if the nanoparticles were stored in the DMEM medium for 10 min, a small amount of magnetic α-Fe_2O_3/Fe_3O_4 nanoparticles had been deposited at the bottom of the bottle. After 48 h, a large number of magnetic α-Fe_2O_3/Fe_3O_4 nanoparticles were deposited at the bottom of the bottle. The magnetic α-Fe_2O_3/Fe_3O_4-CA-CTS-Cur drug delivery nanosystem dispersed very evenly at 10 min and could remain dispersed for a short time. At 24 h and 48 h, a small amount of drug-loaded nanosystem was deposited at the bottom of the bottle, but the bottle could be evenly dispersed by gently shaking it. The above results showed that the prepared magnetic α-Fe_2O_3/Fe_3O_4-CA-CTS-Cur nanoparticles drug delivery system had relatively good dispersion in DMEM medium, and might be applied in the field of nanomedical medicine.

3.3. In vitro study of drug-carrying nanosystems

To explore the effects of different nanomaterials on the viability of SGC-7901 and GES-1 in different environments and to confirm the effectiveness of the drug-loaded nanosystem, the MTT method was adopted to investigate the cytotoxicity of magnetic α-Fe_2O_3/Fe_3O_4 nanoparticles, curcumin, and the α-Fe_2O_3/Fe_3O_4-CA-CTS-Cur nanosystem with or without magnetic field assistance as shown in Fig. 8. Fig. 8A and 8E showed the MTT results obtained when magnetic α-Fe_2O_3/Fe_3O_4 nanoparticles were applied to SGC-7901 and GES-1 cells for 24 h at different concentrations. The results suggested that even at 800 μg/mL, the viability of SGC-7901 cells was up to 95 % and the GES-1 was up to 99 %, indicating that magnetic α-Fe_2O_3/Fe_3O_4 nanoparticles were not toxic to normal and cancer cells at the selected concentration, reflecting the excellent biocompatibility of magnetic α-Fe_2O_3/Fe_3O_4 nanoparticles. Fig. 8B depicted the changes in cell viability of 100 μg/mL magnetic α-Fe_2O_3/Fe_3O_4 nanoparticles with or without a magnetic field over time. The figure clearly described that under the action of a magnetic field, magnetic α-Fe_2O_3/Fe_3O_4 nanoparticles had few impacts on cell viability. This might be because the magnetic field promoted the entrance of more nanomaterials into the cell interior, leading to the induction of cell apoptosis. However, even after 96 h of culture, the viability of SGC-7901 cells was 80 %. In addition, under the same conditions, the survival rate of normal cells GES-1 could reach more than 90 % after 96 h of treatment (Fig. 8F), indicating that the magnetic α-Fe_2O_3/Fe_3O_4 nanoparticles had excellent biological compatibility. It also showed the killing effect of nanoparticles on tumor cells from the side, which might be involved in the iron death pathway mediating apoptosis. Fig. 8C and 8G showed a comparison of the effects of drug-loaded nanosystem with or without magnetic field induction and free curcumin on SGC-7901 and GES-1 cell viability at varying concentrations. As could be seen from the figure, both the drug-loaded nanosystem and free curcumin had concentration-dependent effects on SGC-7901 and GES-1 cells, and the drug-loaded nanosystem under the action of a magnetic field had a stronger inhibitory effect on the viability of SGC-7901 cells than free curcumin, and the drug-loaded nanosystem without the action of a magnetic field. This was because the release of curcumin by the nanosystem was slow. When an identical mole of curcumin was encapsulated in the nanosystem, the actual release amount was lower than that of free curcumin; hence, the inhibitory effect of the drug-loaded nanosystem on cells was not as strong as that of free curcumin. However, under the action of a magnetic field, there was an improved cell localization and uptake of drug-loaded nanosystem. Therefore, more drug-loaded nanosystem entered cells with the action of the magnetic field, and the inhibitory effect on the viabil-

Table 2
Encapsulation efficiency and Drug loading rate of magnetic α-Fe_2O_3/Fe_3O_4-CA-CTS-Cur nanosystem.

	Formula	Argument			Result
		M	M_1	m	
Encapsulation efficiency	$EE = \frac{M-M_1}{M} * 100\%$	20.0 mg	10.3 mg	90.0 mg	48.5 %
Drug loading rate	$LC = \frac{M-M_1}{m+M-M_1} * 100\%$	20.0 mg	10.3 mg	90.0 mg	9.7 %

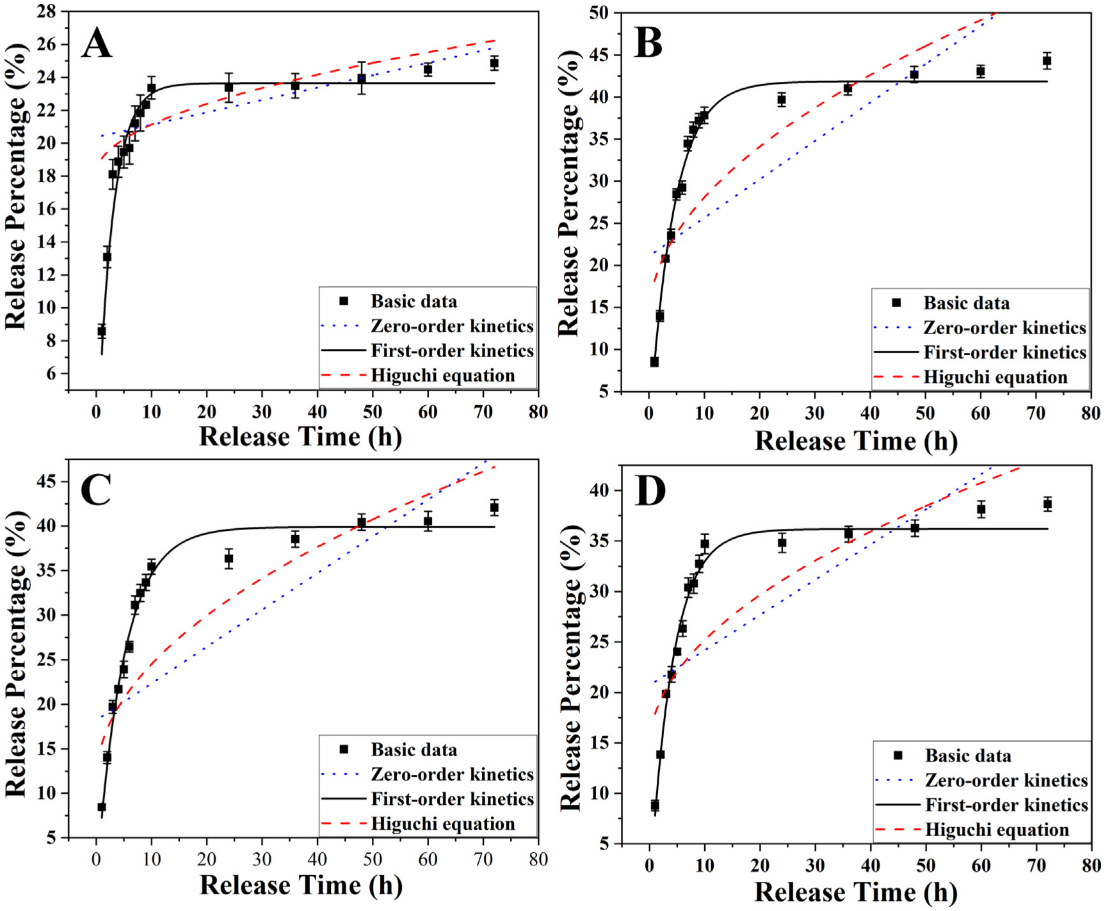

Fig. 7. Fitting curves of the zero-order kinetic model, first-order kinetic model, and Higuchi kinetic model about the heterogeneous magnetic α-Fe_2O_3/Fe_3O_4-CA-CTS-Cur nanosystem release curcumin with the dialysate pH of 1.2 (A), 5.4 (B), 6.8 (C), and 7.4 (D).

Table 3
Fitting parameters of the drug release kinetics of magnetic α-Fe_2O_3/Fe_3O_4-CA-CTS-Cur nanosystem at 37 °C and 100 r/min.

Modal	Parameters	pH			
		1.2	5.4	6.8	7.4
$M_t = a + bt$	a	20.372	21.0818	18.2059	20.7090
	b	0.0752	0.4563	0.4126	0.3486
	R^2	0.2461	0.5799	0.7168	0.7209
$M_t = M * (1 - e^{-k_1 t})$	k_1	0.3610	0.2257	0.2006	0.2425
	M	23.6435	41.8606	39.8931	36.1794
	R^2	0.9593	0.992	0.9875	0.9844
$M_t = ct^{1/2} + d$	c	0.9584	4.6020	4.1542	3.3944
	d	18.1032	13.5018	11.3683	14.4665
	R^2	0.3705	0.7478	0.8464	0.8468

ity of SGC-7901 cells was stronger. At a concentration of 40 μM, the viability of SGC-7901 cells treated with the α-Fe_2O_3/Fe_3O_4-CA-CTS-Cur nanosystem without a magnetic field, free curcumin, and α-Fe_2O_3/Fe_3O_4-CA-CTS-Cur nanosystem under magnetic field were 83 %, 66 %, and 57 %, respectively. In addition, the inhibitory effect of the drug-loaded nanosystem on SGC-7901 cells showed a relatively uniform concentration dependence regardless of the magnetic field, while the effect of free curcumin on SGC-7901 cells was not very strong at lower than 20 μM. However, when the concentration of free curcumin reached 40 μM, SGC-7901 cell viability decreased significantly, which may be attributed to the low solubility and poor stability of curcumin. In addition, the α-Fe_2O_3/

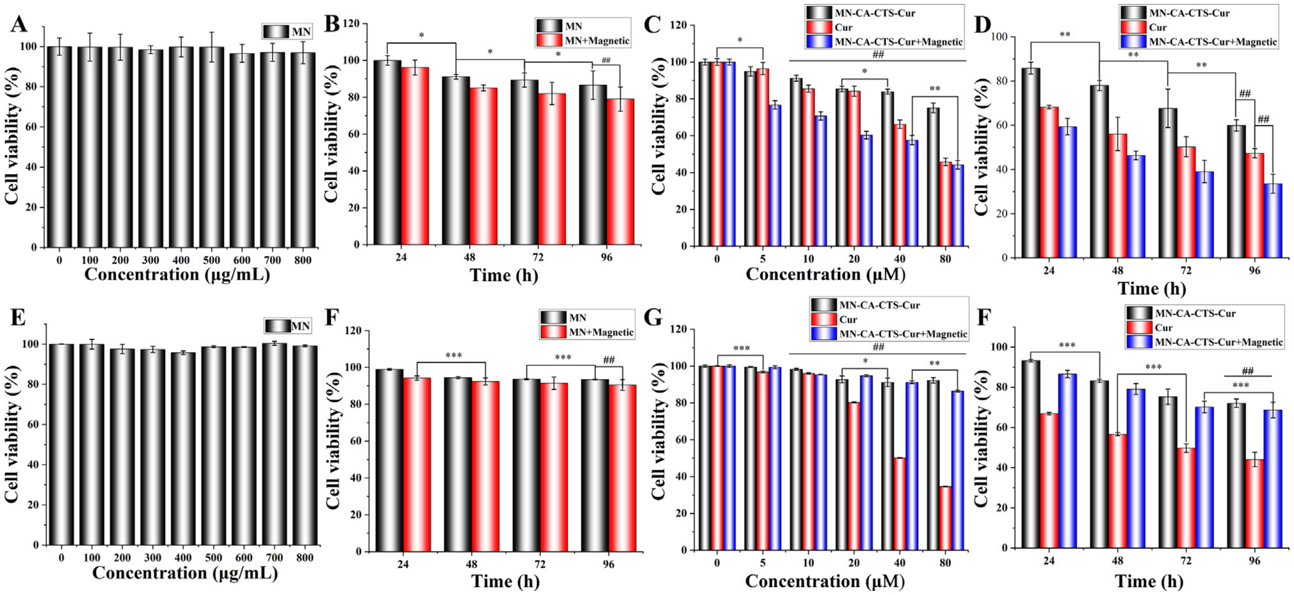

Fig. 8. Toxicity of gastric cancer cells (SGC-7901) (A-D) and normal cells (GES-1) (E-H) in vitro. Cytotoxicity of (A and B) the heterogeneous magnetic α-Fe_2O_3/Fe_3O_4 nanoparticles (MN) at different concentrations. Cytotoxicity of MN (100 μg/mL) at different treatment times, with or without magnetic field (B and F). Cytotoxicity of MN-CA-CTS-Cur nanosystem, curcumin, and MN-CA-CTS-Cur nanosystem assisted by a magnetic field at different concentrations (C and G), and MN-CA-CTS-Cur nanocarriers, curcumin, MN-CA-CTS-Cur nanocarriers assisted by a magnetic field at the concentration of 40 μM for different period times (D and H). (n = 3, $^*P < 0.05$, comparison within groups; $^{**}P < 0.01$, $^{***}P < 0.001$ comparison within groups; ##P < 0.01, comparison among groups).

Fe_3O_4-CA-CTS-Cur nanosystem continuously released curcumin, thereby exerting a continuous inhibitory effect on SGC-7901 cells. Therefore, a drug-loaded nanosystem could not only improve the inhibitory effect of curcumin on SGC-7901 cells but also improve its stability in practical applications. However, in normal cells, free curcumin exhibited strong cytotoxicity, and this greatly limited the application of curcumin in vivo. Surprisingly, nanoparticles loaded with curcumin could effectively resist the cytotoxic effects brought by free curcumin, could greatly improve biocompatibility, and showed a strong ability to be applied in vivo.

Fig. 8D and 8H showed that cell viability changed over time when 40 μM α-Fe_2O_3/Fe_3O_4-CA-CTS-Cur nanosystem and free curcumin were applied to SGC-7901 and GES-1 cells. The effect of the magnetic α-Fe_2O_3/Fe_3O_4-CA-CTS-Cur nanosystem on SGC-7901 cells was time-dependent, with or without a magnetic field. Free curcumin also inhibited the viability of SGC-7901 cells in a time-dependent manner. The survival rate of the α-Fe_2O_3/Fe_3O_4-CA-CTS-Cur nanosystem to SGC-7901 cells treated for 96 h under a magnetic field was 33 %, indicating that the prepared α-Fe_2O_3/Fe_3O_4-CA-CTS-Cur nanosystem had an excellent ability to inhibit SGC-7901 cell viability under the action of the magnetic field. After 96 h, the survival rate of the α-Fe_2O_3/Fe_3O_4-CA-CTS-Cur nanosystem to GES-1 cell still reached up to 70 %, showing that while killing tumor cells, normal cells would also be damaged, but the survival rate of normal cells had been greatly improved, and the toxic side effects of drugs had been greatly reduced.

To investigate the inhibitory effect of the drug-loaded nanosystem on cell migration as shown in Fig. 9, the expression of CD44 protein in SGC-7901 cells was investigated under the action of the heterogeneous magnetic α-Fe_2O_3/Fe_3O_4 nanoparticles, curcumin, and α-Fe_2O_3/Fe_3O_4-CA-CTS-Cur nanosystem with magnetic field, and the results were displayed in Fig. 9A and S4. The figures showed that the CD44 protein, which was an adhesion molecule, was highly expressed in the control cancer cells. Because the CD44 protein not only promoted the growth of tumor cells but also played a significant role in the invasion and migration of SGC-7901 cells, a high expression level of CD44 promoted the development of cancer (Zer et al., 2023). After the treatment of SGC-7901 cells with the three drugs, the expression level of CD44 protein decreased successively, and the drug-loaded nanosystem had the strongest inhibitory effect on CD44 expression under the magnetic field. These results indicated that drug-loaded nanosystem could significantly reduce the expression level of CD44 protein under a magnetic field, suggesting that they might inhibit the proliferation and migration of tumor cells. Therefore, a scratch experiment was employed to visually examine the inhibitory effect of α-Fe_2O_3/Fe_3O_4-CA-CTS-Cur nanosystem, under a magnetic field, on the migration of SGC-7901 cells. Fig. 9C and 9D displayed the comparison results of scratch experiments in the control group and the α-Fe_2O_3/Fe_3O_4-CA-CTS-Cur nanosystem (40 μM) assisted by a magnetic field. It was observed that the drug-loaded nanosystem assisted by the magnetic field significantly inhibited cell migration. The scratches in the control group became increasingly narrow in the cell culture stage, whereas those in the drug-loaded nanosystem assisted by the magnetic field group were almost twice as wide as those in the control group. In addition, the cell density in the control group was high, and the cells gradually migrated to scratch. However, in the α-Fe_2O_3/Fe_3O_4-CA-CTS-Cur nanosystem assisted by the magnetic field, the gaps between cells were visible, and the cell density was much lower than that of the control group. Therefore, the α-Fe_2O_3/Fe_3O_4-CA-CTS-Cur nanosystem, assisted by a magnetic field, not only inhibited the migration of SGC-7901 cells but also had a marked inhibitory effect on cancer cell proliferation. In conclusion, the α-Fe_2O_3/Fe_3O_4-CA-CTS-Cur nanosystem, assisted by a magnetic field, had great inhibitory potential against SGC-7901 cells.

MGCE generated electron transfer between the anionic probe in the electrolyte and the electrode surface, resulting in the appearance of electrode potential. After treating the cells with the different test nanomaterials, they were co-incubated and connected to the electrode surface, and the change in potential was detected to determine if there was uptake of nanomaterials by the cells. Fig. 9B showed the cyclic voltammetry curve of the MGCE electrode co-incubated with cells treated with the different test nanomaterials. From the curve, the smallest current response was observed in the control group without drug action because the sur-

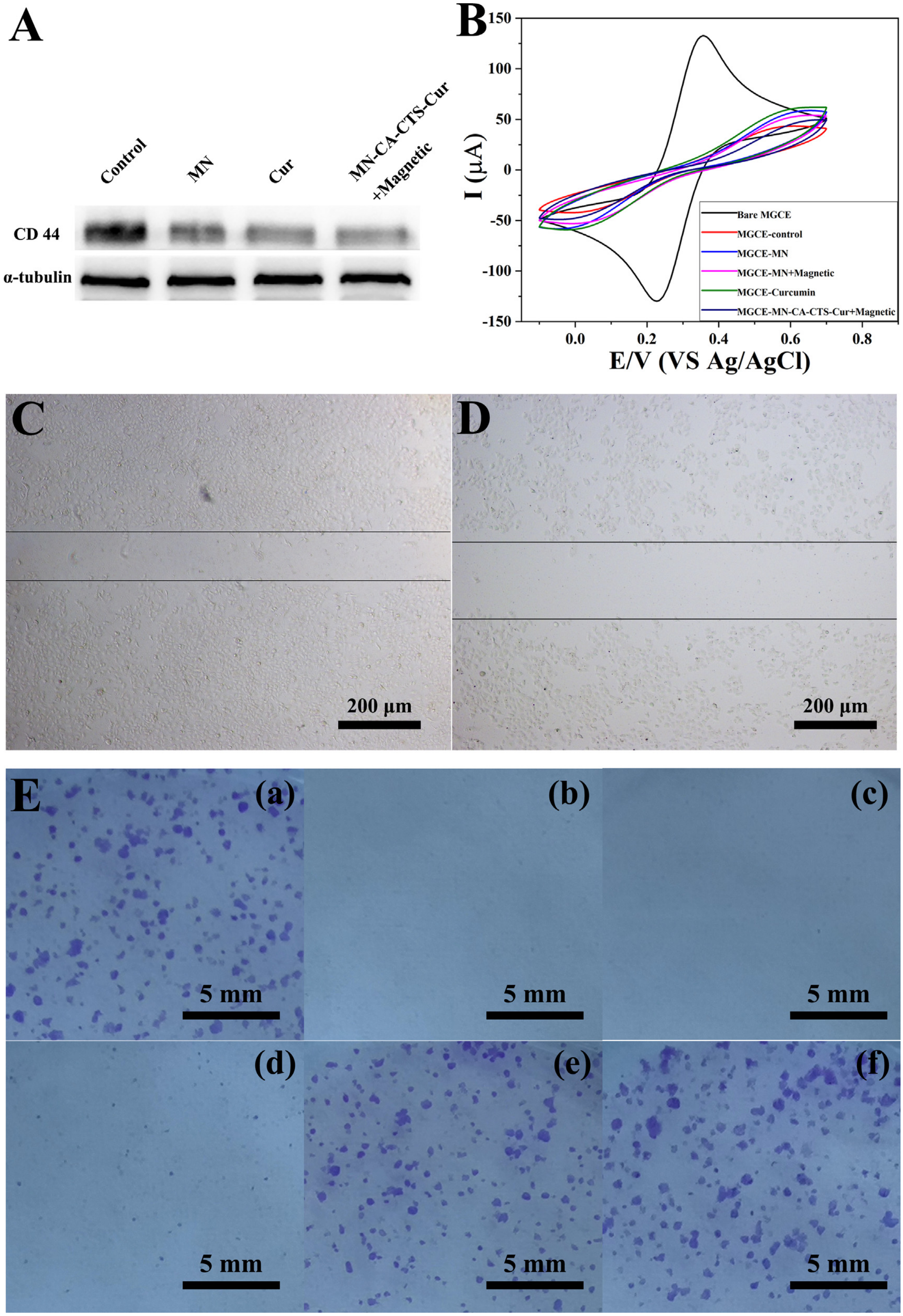

Fig. 9. CD44 expression of SGC-7901 cells (A). CV curves of the bare electrode, electrode with cells (control), the electrode with cells MN-treated cells, the electrode with MN-treated cells assisted with a magnetic field, the electrode with curcumin-treated cells, electrode, and cells treated with MN-CA-CTS-Cur nanocarriers assisted with magnetic field (B). the scratch wound of control group (C) and MN-CA-CTS-Cur nanocarriers assisted by a magnetic field (D). Colony formation assay results (E) of SGC-7901 cells treated with blank (a), MN-CA-CTS-Cur nanosystem assisted by a magnetic field (b), MN-CA-CTS-Cur nanosystem (c), curcumin (d), MN assisted by a magnetic field (e) and MN (f).

face of the electrode was attacked by cancer cells after incubation with the cells. The negative charge density on the surface of normal cancer cells was high; hence, the anionic probe in the solution had less contact with the surface of the MGCE electrode owing to electrostatic repulsion. In addition, the presence of cancer cells on the surface of the electrode also caused steric hindrance, making it difficult for the anionic probe to reach the surface of the MGCE electrode for electron transfer. Therefore, the current response was the lowest. However, for α-Fe_2O_3/Fe_3O_4-CA-CTS-Cur nanosystem under magnetic field auxiliary treatment of SGC-7901 cells, the potential slightly increased. This was because, under the magnetic field condition, SGC-7901 cells absorbed more α-Fe_2O_3/Fe_3O_4-CA-CTS-Cur nanosystem, which destroyed the cell integrity. Some α-Fe_2O_3/Fe_3O_4-CA-CTS-Cur nanosystem adhered to the cell surface and neutralized some of the negative potentials, and the electrostatic repulsion decreased slightly, resulting in a slight increase in the current response in the control group. Greater cell uptake was observed for heterogeneous α-Fe_2O_3/Fe_3O_4 nanoparticles with a magnetic field than that without the magnetic field. Moreover, the positive potential on the surface of the magnetic nanoparticles was strong, which neutralized the negative potential on the cell surface to a greater extent, such that more anionic probes could reach the surface of the MGCE electrode. However, steric hindrance also increased simultaneously. Therefore, under the combined action of the increase in steric hindrance and a decrease in electrostatic repulsion, the current response of α-Fe_2O_3/Fe_3O_4 nanoparticle assisted by the magnetic field was between the response of the drug-loaded nanosystem assisted by the magnetic field and that of the bare α-Fe_2O_3/Fe_3O_4 nanoparticle group. For the group of cells treated with heterogeneous magnetic α-Fe_2O_3/Fe_3O_4 nanoparticles and incubated on the surface of the MGCE electrode, the negative potential on the cell surface was slightly neutralized by the positively charged magnetic nanomaterials. Moreover, due to the low uptake of magnetic nanomaterials by SGC-7901 cells, the steric hindrance caused by the magnetic α-Fe_2O_3/Fe_3O_4 nanoparticles was also small. Therefore, the current response of magnetic α-Fe_2O_3/Fe_3O_4 nanoparticles was higher when the cells were treated without a magnetic field than that of cells treated with a magnetic field. Among all the experimental groups, the group treated with curcumin showed the highest current response on the co-incubated MGCE electrode. This was possibly caused by the destruction of the cell membrane of some SGC-7901 cells after treatment with free curcumin, which resulted in reduced electrostatic repulsion. However, in comparison with the bare MGCE electrode, the current response performance declined because the curcumin had a negative charge, and the surface of some SGC-7901 cells was negative. The negative charge and the anionic probe in the electrolyte were mutually exclusive, leading to less contact with the surface of the MGCE electrode probe and a lower current response.

The proliferation ability and population dependence of SGC-7901 cells treated with the different test samples were evaluated using cell cloning experiments. Fig. 9E showed the results of the gastric cancer colony formation experiment after 10 days in the control group (a), 40 μM α-Fe_2O_3/Fe_3O_4-CA-CTS-Cur nanosystem assisted by magnetic field group (b), 40 μM α-Fe_2O_3/Fe_3O_4-CA-CTS-Cur nanosystem without magnetic field group (c), 40 μM free curcumin group (d), 100 μg/mL α-Fe_2O_3/Fe_3O_4 nanoparticles assisted by magnetic field (e), and α-Fe_2O_3/Fe_3O_4 nanoparticles without magnetic field group (f). As observed in the control group, SGC-7901 cells with adhered growth could proliferate and form colonies. As shown in Fig. 9E(f), the colony-forming ability of the α-Fe_2O_3/Fe_3O_4 nanoparticles group was almost the same as that of the control group, indicating that α-Fe_2O_3/Fe_3O_4 nanoparticles exerted a slight effect on SGC-7901 cells and had strong biocompatibility, which was consistent with the MTT results. As shown in Fig. 9E(e), after the magnetic α-Fe_2O_3/Fe_3O_4 nanoparticles were applied to SGC-7901 cells under the action of a magnetic field, the number of small colonies generated was higher than that of large colonies. This was possible because the magnetic field promoted the uptake of magnetic α-Fe_2O_3/Fe_3O_4 nanoparticles by SGC-7901 cells, which reduced cell proliferation. Fig. 9E(b) and 9E(c) showed colony formation in SGC-7901 cells treated with the α-Fe_2O_3/Fe_3O_4-CA-CTS-Cur nanosystem with and without magnetic field induction. The drug-loaded nanosystem could completely inhibit cell survival for a long time with or without the magnetic field. SGC-7901 cells treated with free curcumin had several small colonies (Fig. 9E(d)) possibly because SGC-7901 cells became resistant to curcumin under long-term drug action. This result was slightly different from that of the MTT assay because the maximum duration of treatment in the MTT assay was only 96 h; hence, the short-term action of the drug was deficient to trigger the resistance of cancer cells to free curcumin (Jin et al., 2020). However, in the cell colony formation experiment, the 10-day induction period allowed the stronger cells to survive and develop drug resistance; hence, small colonies were observed in this group. The drug-loaded nanosystem had a sustained and long-term effective inhibitory effect on the proliferation of SGC-7901 cells. Therefore, the α-Fe_2O_3/Fe_3O_4-CA-CTS-Cur nanosystem prepared in this study not only had a good ability to inhibit the proliferation of SGC-7901 cells but also reduced resistance to anticancer drugs. The latter aspect was worthy of in-depth research in the field of anticancer therapy.

Fig. 10A depicted the AO-EB staining diagram of SGC-7901 cells treated with DMEM, magnetic α-Fe_2O_3/Fe_3O_4 nanoparticles, magnetic α-Fe_2O_3/Fe_3O_4 nanoparticles with magnetic field assistance, curcumin, α-Fe_2O_3/Fe_3O_4-CA-CTS-Cur nanosystem with magnetic field assistance, and α-Fe_2O_3/Fe_3O_4-CA-CTS-Cur nanosystem. As could be seen from the first three groups, the effect of 100 μg/mL magnetic α-Fe_2O_3/Fe_3O_4 nanoparticles, with or without a magnetic field, on the apoptosis of SGC-7901 cells was similar to that of the control group, which was negligible. Apoptosis was observed in SGC-7901 cells treated with 40 μM curcumin. The early apoptotic cells (round green shape) and a small number of late apoptotic cells (orange) were clearly shown in Fig. 10A. In the 40 μM drug-loaded nanosystem assisted by magnetic field treatment group, the number of cells in the early and late apoptotic states significantly increased, and they were visible. Moreover, a small number of necrotic cells could also be observed, suggesting that it had a stronger ability to promote the apoptosis of SGC-7901 cells than free curcumin. However, compared with those in the free curcumin group, the early and late apoptotic cells with ball-shaped morphology were reduced in the drug-loaded nanosystem group with no magnetic field induction (Kuang et al., 2021). These results indicated that 40 μM of α-Fe_2O_3/Fe_3O_4-CA-CTS-Cur nanosystem, without magnetic field localization, or the free curcumin could not promote the apoptosis of SGC-7901 cells as the nanosystem with the magnetic field, which was expected and consistent with the MTT results.

The inhibition of cancer cell growth through apoptosis was a common drug effect as shown in Fig. 10. Annexin V-FITC and PI double staining were used to detect apoptosis induced by the α-Fe_2O_3/Fe_3O_4-CA-CTS-Cur nanosystem. Fig. 10B and S5 showed the apoptosis of the control group (B1), 100 μg/mL magnetic α-Fe_2O_3/Fe_3O_4 nanoparticles group (B2), 40 μM free curcumin group (B3), and 40 μM α-Fe_2O_3/Fe_3O_4-CA-CTS-Cur nanosystem magnetic field-assisted group (B4). As revealed in Fig. 10(B1), the proportion of living SGC-7901 cells after undergoing the whole staining process was 90.18 %. As shown in Fig. 10(B2), the proportion of living cells in the group treated with the magnetic α-Fe_2O_3/Fe_3O_4 nanoparticles was only 82.35 %. The low proportion of living cells in the α-Fe_2O_3/Fe_3O_4 nanoparticles group could be attributed to

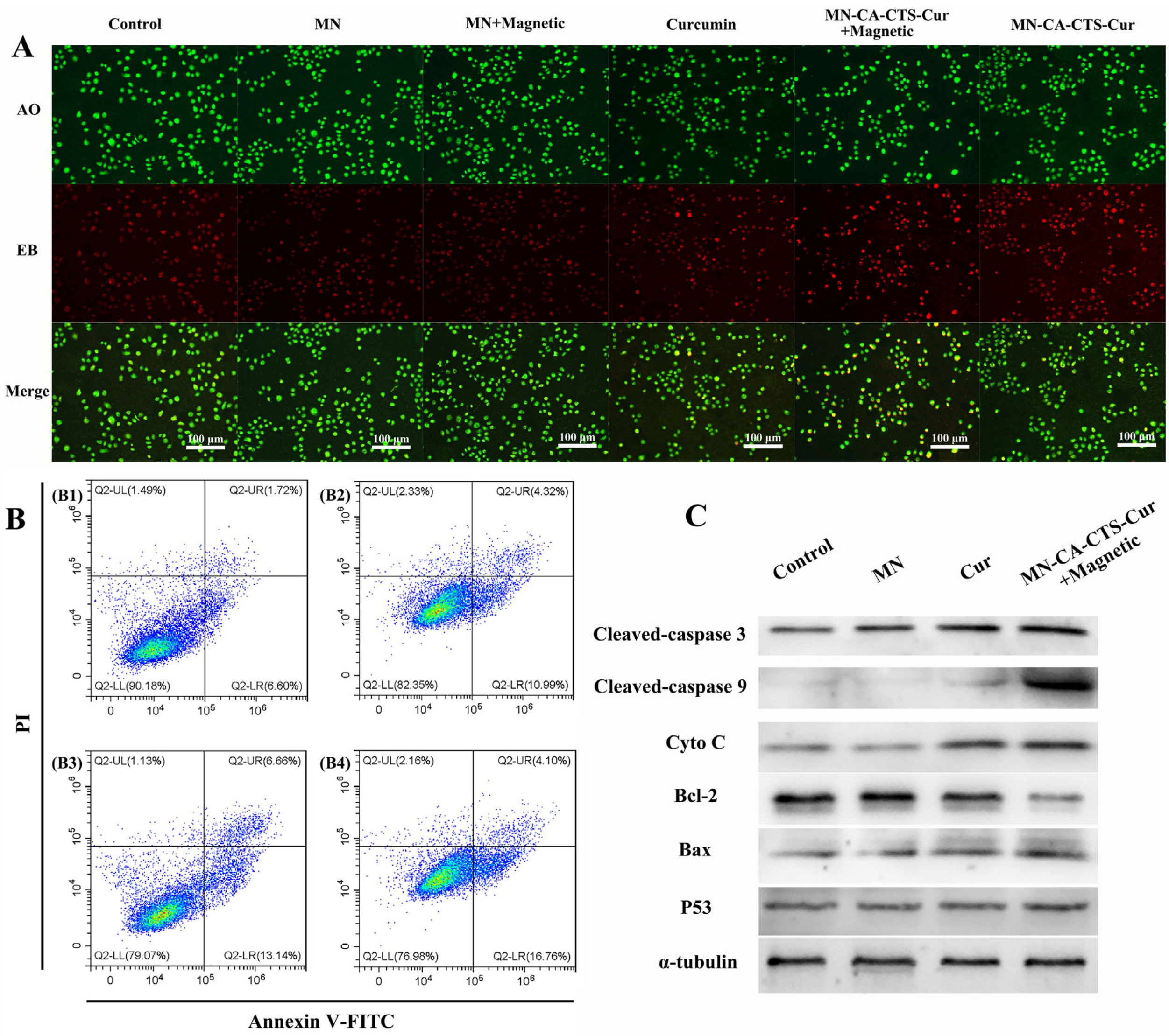

Fig. 10. Acridine orange-ethidium bromide double staining fluorescence pictures (A) of SGC-7901 cells treated with blank, α-Fe_2O_3/Fe_3O_4 nanoparticles (MN), MN assisted by a magnetic field, curcumin, MN-CA-CTS-Cur nanosystem assisted by magnetic field, MN-CA-CTS-Cur nanosystem. Annexin V-FITC/propidium iodide flow cytometry analysis (B) of SGC-7901 cells treated with blank, MN, curcumin, and α-Fe_2O_3/Fe_3O_4-CA-CTS-Cur nanosystem assisted by a magnetic field. Western blot analysis (C) of SGC-7901 cells treated with the different test materials.

the limited uptake of magnetic nanomaterials by cells, as most of the nanomaterials were on the outside of the cells. Therefore, when the nanomaterials that did not enter the cells were washed away by PBS, some cells died due to mechanical damage, and the proportion of living cells in the magnetic α-Fe_2O_3/Fe_3O_4 nanoparticles group was less than that in the control group. The group treated with a drug-loaded nanosystem under the influence of a magnetic field exhibited a higher number of cells undergoing apoptosis compared to the group treated with free curcumin (Fig. S5). Specifically, the percentage of SGC-7901 cells in the early apoptosis stage increased significantly by up to 16.76 % after 24 h. These results indicated that the drug-loaded nanosystem mainly caused programmed injury and death of SGC-7901 cells. In the free curcumin group, the early apoptosis of SGC-7901 cells was relatively low, whereas the late apoptotic and necrotic cells were relatively higher. Programmed cell death did not cause inflammation and had minimal effects on surrounding cells. Therefore, the α-Fe_2O_3/Fe_3O_4-CA-CTS-Cur nanosystem assisted by a magnetic field, which was mainly used to induce programmed death of SGC-7901 cells, could not only improve the anticancer effect of curcumin but also reduce the side effects. To further investigate the molecular mechanism of the α-Fe_2O_3/Fe_3O_4-CA-CTS-Cur nanosystem on SGC-7901 cells under a magnetic field condition, the expression of various proteins in SGC-7901 cells was investigated. Fig. 10C and S6 displayed the expression of key proteins in the caspase pathway. As could be seen from the figures, when the drug-loaded nanosystem stimulated SGC-7901 cells under the action of a magnetic field, the expression level of P53 significantly increased, compared with that in the other groups. As P53 could promote the expression of Bax, it could be seen in Fig. 10C that the amount of Bax/Bcl-2 in the drug-loaded nanosystem assisted by the magnetic field was significantly higher than that in the other groups, revealing that the α-Fe_2O_3/Fe_3O_4-CA-CTS-Cur nanosystem had a stronger apoptotic effect under the magnetic field condition. With a high expression level of the pro-apoptotic protein, cytochrome *C* was gradually released into the cytoplasm through the mitochondrial outer membrane channel (Gao et al., 2019; Wang et al., 2017), resulting in the maximum expression level of cytochrome *C* in the magnetic field-assisted α-Fe_2O_3/Fe_3O_4-CA-CTS-Cur nanosystem. The high expression level of cytochrome *C* caused a caspase cascade reaction, which increased the level of apoptosis.

Caspase 9 was a priming caspase, and most of it appeared in the form of pro-caspase 9 with minimal apoptotic stimulation (Wang et al., 2019). Therefore, the cleaved-caspase 9 content was low in the control group and the magnetic α-Fe_2O_3/Fe_3O_4 nanoparticles group. However, in the drug-loaded nanosystem with the magnetic field-assisted group, the activation of cleaved-caspase 9 was significantly high because its effect on SGC-7901 cells was more intense and its apoptotic effect was higher than that of free curcumin (Gan et al., 2022; Li et al., 2020). The associated mechanism was illustrated in Scheme 2. In addition, the expression level of cleaved-caspase 3 in the α-Fe_2O_3/Fe_3O_4-CA-CTS-Cur nanosystem assisted by the magnetic field was approximately 2.5 folds higher than that for the control group (Fig. 10C). These results suggested that drug-loaded nanosystem could significantly increase caspase 3 activation and promote cell apoptosis. In addition, the α-Fe_2O_3/Fe_3O_4-CA-CTS-Cur nanosystem assisted by a magnetic field had a significantly higher inhibitory effect on anti-apoptotic proteins and promoted the expression of other proteins conducive to apoptosis than single ferrite and free curcumin. The results indicated that the α-Fe_2O_3/Fe_3O_4-CA-CTS-Cur nanosystem designed in this experiment could combine the advantages of single ferrite and free curcumin for improved pro-apoptotic effect. These results confirmed that the α-Fe_2O_3/Fe_3O_4-CA-CTS-Cur nanosystem could induce apoptosis through the caspase pathway in the presence of a magnetic field.

To confirm that the prepared nanosystem played a role after entering the cells as shown in Fig. 11, Prussian blue staining was used to stain the cells treated with the different test nanomaterials (Fig. 11A). As revealed in Fig. 11(A1), the SGC-7901 cells presented an epithelioid structure. Fig. 11(A2) showed the Prussian blue staining results of SGC-7901 cells treated with 100 μg/mL magnetic α-Fe_2O_3/Fe_3O_4 nanoparticles. A small number of cells were observed with blue particles inside, as indicated by the arrow in the figure. This indicated that the magnetic α-Fe_2O_3/Fe_3O_4 nanoparticles could also enter the cell interior, but the amount that entered was limited. Fig. 11(A3) showed SGC-7901 cells treated with 40 μM free curcumin; a small number of cells were damaged, with their contents spilled, and cells with volume shrinkage were also observed. The effect of free curcumin on SGC-7901 cell death was also explored. Fig. 11(A4) showed the Prussian blue staining results of SGC-7901 cells treated with 40 μM α-Fe_2O_3/Fe_3O_4-CA-CTS-Cur nanosystem assisted with a magnetic field. The results showed that many cells incorporated the blue compound. As be seen from the magnified image in the lower left corner of Fig. 11 (A4), SGC-7901 cells incorporated a large amount of the drug-loaded nanosystem, confirming the assertion that drug-loaded nanosystem entered the cell and played a role. Moreover, many pyknotic cells could be observed in the figure, indicating that a drug-loaded nanosystem assisted by a magnetic field could promote the apoptosis of SGC-7901 cells.

The results of the Prussian blue staining confirmed that iron was present in the cells treated with the drug-loaded nanosystem. Therefore, to further explore the mechanism, the levels of ferroptosis-related proteins in the cells after drug treatment were determined (Fig. 11B). As shown in Fig. 11C, D, and E after the cells were treated with 40 μM curcumin and α-Fe_2O_3/Fe_3O_4-CA-CTS-Cur nanosystem assisted by magnetic field, the levels of FTH1 and GPX4 decreased significantly, compared with those in the control and magnetic α-Fe_2O_3/Fe_3O_4 nanoparticles group. Moreover, the lowest levels of the two proteins were observed in SGC-7901 cells treated with the drug-loaded nanosystem under a magnetic field condition. FTH1 deficiency led to the destruction of iron homeostasis in cells, and the increase in iron content in cells was conducive to ferroptosis. GPX4 was one of the most important antioxidant enzymes associated with ferroptosis. Therefore, low GPX4 levels inhibited the ability of cells to reduce peroxide bonds, which increased toxic peroxide lipids and reactive oxygen species in cells and ultimately caused cell death. Free curcumin also significantly stimulated lipid peroxidation, and FTH1 and GPX4 were downregulated in the free curcumin group, but the effect was not as strong as that in the drug-loaded nanosystem group with magnetic field assistance (Mou et al., 2019; H.Y. Wang et al., 2021). As shown in Fig. 11D, the activity of COX2 increased significantly in the presence of free curcumin and drug-loaded nanosystem assisted by a magnetic field. This triggered an inflammatory response within the cell, which in turn induced cell death. The induction effect of free curcumin on COX2 was slightly stronger than that of the drug-loaded nanosystem assisted by the magnetic field possibly because free curcumin did not only show anticancer and anti-inflammatory functions but also needed antioxidant effects. After direct contact with SGC-7901 cells, they entered the cells and stimulated oxidative stress responses in a variety of ways, and in a short period, the concentration of free curcumin became very high, and more COX2 was produced. However, the amount of COX2 produced in the drug-loaded nanosystem assisted by magnetic field-treated SGC-7901 cells was also about threefold higher than that of the control group. The mechanism was illustrated in Scheme 2. These results confirm that the drug-loaded nanosystem could induce cell death through the ferroptosis pathway (Kong et al., 2021; Zhu et al., 2021).

MDA was a natural product of lipid oxidation in living organisms as shown in Fig. 12. When there was oxidative stress in cells, lipid peroxidation occurred owing to the action of free radicals. After oxidation, some fatty acids gradually decomposed into a series of complex compounds, including MDA (Wang et al., 2018). Therefore, MDA had been widely applied as an indicator of lipid oxidation. Fig. 12A showed the expression levels of MDA in SGC-7901 cells treated with 100 μg/mL magnetic α-Fe_2O_3/Fe_3O_4 nanoparticles, 40 μM α-Fe_2O_3/Fe_3O_4-CA-CTS-Cur assisted with NAC (5 mM) (Lu et al., 2016) and magnetic field, 40 μM curcumin, 40 μM α-Fe_2O_3/Fe_3O_4-CA-CTS-Cur nanosystem, and 40 μM α-Fe_2O_3/Fe_3O_4-CA-CTS-Cur nanosystem assisted with a magnetic field. The MDA content of the control group and the magnetic α-Fe_2O_3/Fe_3O_4 nanoparticles group changed slightly after they were treated with SGC-7901 cells, indicating that magnetic α-Fe_2O_3/Fe_3O_4 nanoparticles hardly increased the level of lipid peroxidation in SGC-7901 cells. Drug-loaded nanosystem with or without the help of a magnetic field could produce strong lipid peroxidation, even higher than that under the action of free curcumin, probably because of the release of iron ions by ferrite in the drug-loaded nanosystem and the increase in intracellular lipid peroxidation induced by ferroptosis. MDA not only affected the mitochondrial respiratory chain and its key enzymes but also aggravated membrane damage when its expression level increased (Du et al., 2019). Therefore, the drug-loaded nanosystem had the most intense damage effect on SGC-7901 cells assisted by a magnetic field. NAC was an antioxidant that protects cells from the damage caused by oxidative stress. Therefore, the addition of NAC significantly reversed the mediating effect of the drug-loaded nanosystem assisted by the magnetic field on cell oxidative stress, which confirmed that a drug-loaded nanosystem assisted by a magnetic field could promote cell oxidation and cause cell damage.

Superoxide dismutase (SOD) was a metalloprotease present in living organisms. It catalyzed the disproportionation of superoxide anion radicals, generated hydrogen peroxide and oxygen, and played a crucial role in the balance between oxidative stress and the antioxidant system (Kumar and Clair, 2021). The reduction in SOD level could weaken the inhibitory effect of superoxide anion free radicals and cause cancer cell damage. Fig. 12B showed SOD

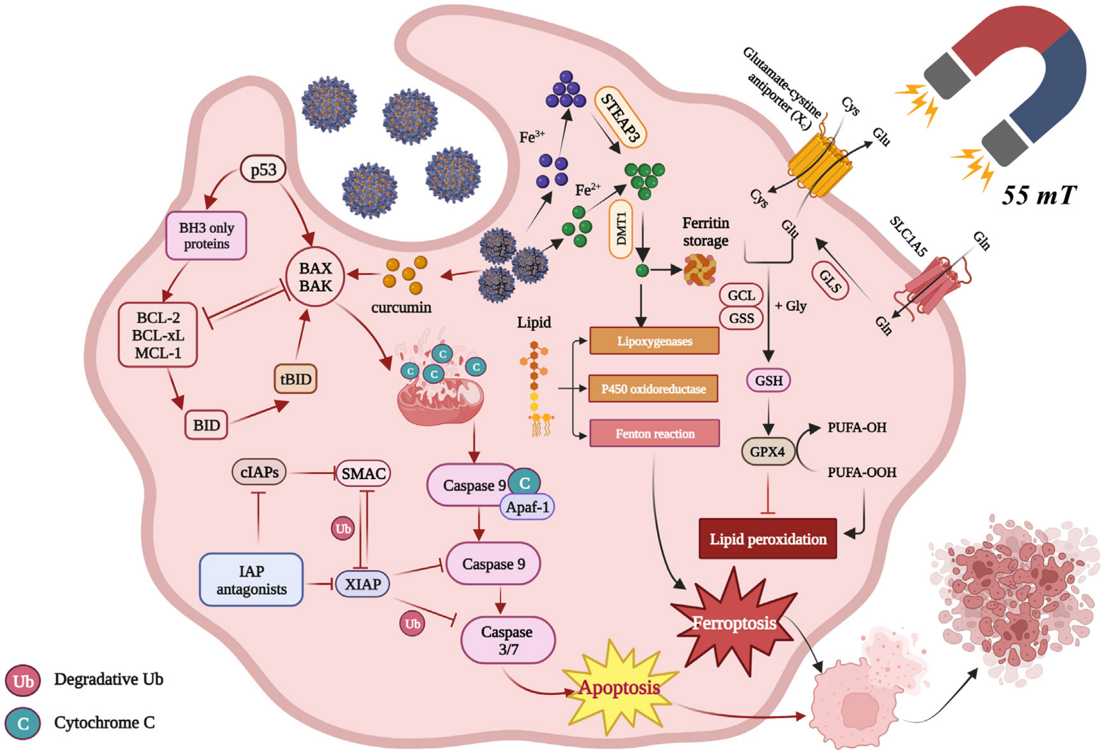

Scheme 2. Schematic diagram of the mechanism of action of the heterogeneous magnetic α-Fe_2O_3/Fe_3O_4-CA-CTS-Cur nanosystem.

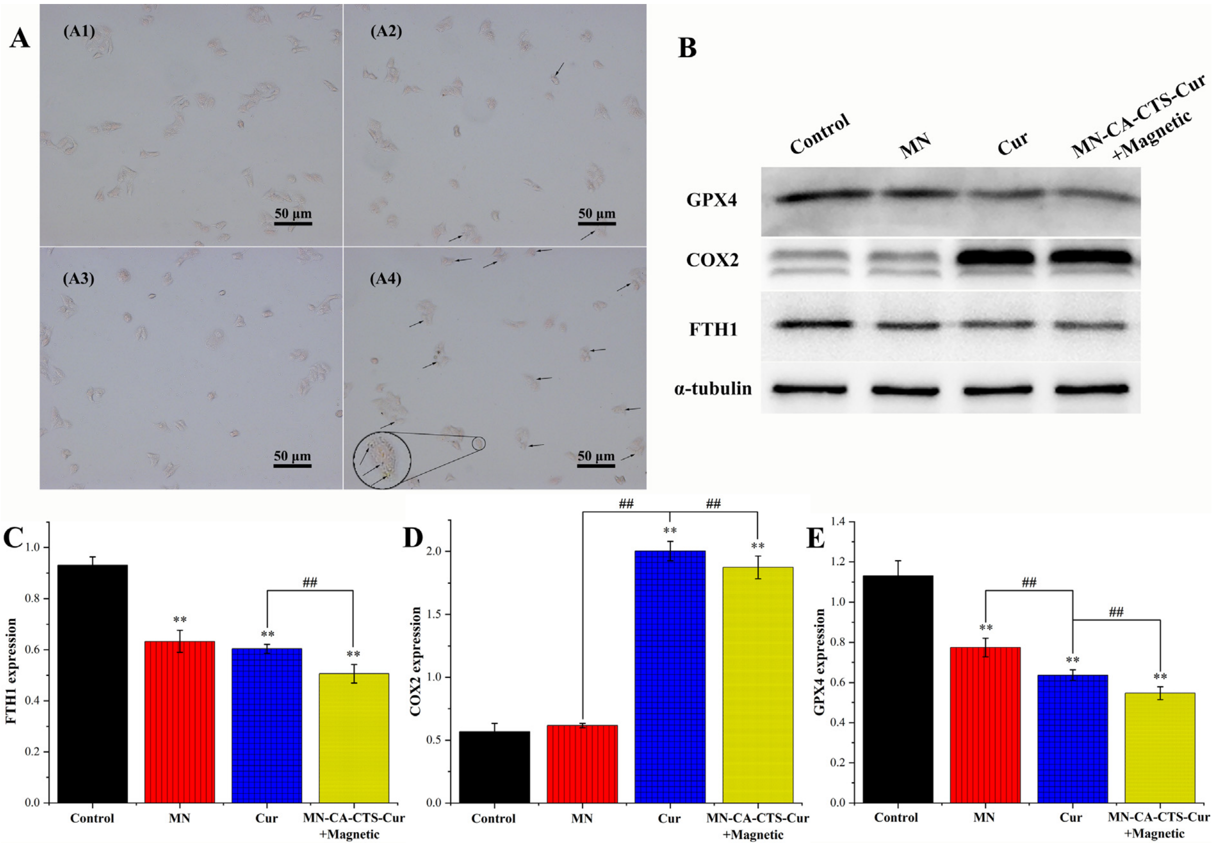

Fig. 11. Prussian blue staining experiment (A) of SGC-7901 cells treated with blank (A1), α-Fe_2O_3/Fe_3O_4 nanoparticles (A2), curcumin (A3), and MN-CA-CTS-Cur nanosystem (A4) assisted by a magnetic field. Western blot analysis (B) of SGC-7901 cells induced by the different test materials. Relative expression levels of FTH1 (C), COX2 (D), GPX4 (E). (n = 3, $^{**}P < 0.01$, comparison within groups; $^{\#\#}P < 0.01$, comparison among groups).

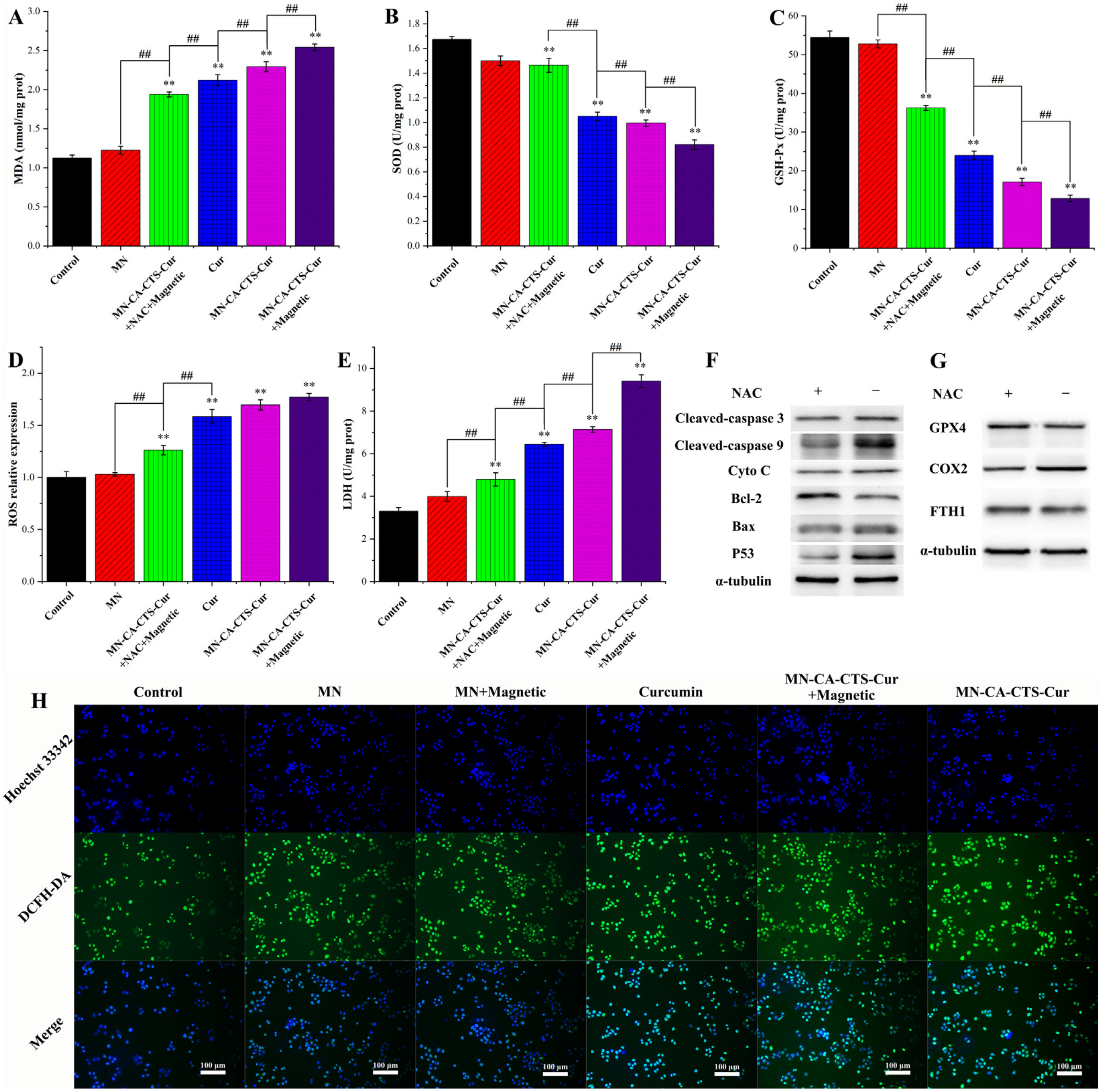

Fig. 12. Malondialdehyde (MDA) (A), superoxide dismutase (SOD) (B), glutathione peroxidase (GSH-Px) (C), reactive oxygen species (ROS) (D), and lactate dehydrogenase (LDH) levels (E) of SGC-7901 cells treated with blank, α-Fe_2O_3/Fe_3O_4 nanoparticles (MN), MN-CA-CTS-Cur nanosystem with magnet and NAC, Cur, MN-CA-CTS-Cur nanosystem, and MN-CA-CTS-Cur nanosystem assisted by magnetic field. The expression levels of apoptosis-related proteins (F) and ferroptosis-related proteins (G) before and after NAC treatment. ROS in SGC-7901 detected by DCFH-DA probe (H). (n = 3, $^{**}P < 0.01$, comparison within groups; $^{\#\#}P < 0.01$, comparison among groups).

expression in SGC-7901 cells under six different conditions. The SOD content in the control group was the highest because SGC-7901 cells produced many free radicals during rapid growth. Next, the cells spontaneously increased the SOD content to maintain rapid growth and balance the generation and elimination of free radicals, which was conducive to cell growth. After adding NAC, the SOD content in the cells of the drug-loaded nanosystem under a magnetic field increased significantly, compared with that in cells not treated with NAC. This was because NAC could increase the capture of free radicals in cells, leading to the spontaneous generation of more SOD in SGC-7901 cells to offset the influence of drug-loaded nanosystem assisted with a magnetic field and eliminate more free radicals, and this was conducive to the survival of SGC-7901 cells. In the free curcumin and drug-loaded nanosystem with or without magnetic field assistance, the inhibitory ability of SOD was strong. The drug-loaded nanosystem with a magnetic field inhibited SOD production in SGC-7901 cells, and the SOD expression level was more than two times lower than that in the control group. These results indicated that the α-Fe_2O_3/Fe_3O_4-CA-CTS-Cur nanosystem, under the action of a magnetic field, could help to disrupt the balance of free radical production and scavenging in SGC-7901 cells and reduce SOD, leading to an increased free radical content and cell damage.

Glutathione peroxidase (GSH-Px) was an important enzyme that catalyzed the decomposition of hydrogen peroxide. It could catalyze the conversion of glutathione (GSH) to oxidized glutathione (GSSG) and reduce toxic peroxides to non-toxic hydroxyl compounds, which could play a role in protecting the structure and functional integrity of cell membranes (M.L. Zhang et al., 2020; Feng et al., 2016; H.Y. Zhang et al., 2020). Fig. 12C depicted the changes in GSH-Px content in SGC-7901 cells under the effects of six different test nanomaterials. The changes of GSH-Px in SGC-7901 cells were minimal after treatment with magnetic α-Fe_2O_3/Fe_3O_4 nanoparticles. This was due to the strong biocompatibility of magnetic α-Fe_2O_3/Fe_3O_4 nanoparticles and the low intake of magnetic nanomaterials by SGC-7901 cells. Therefore, the original physiological balance of the cells was not damaged after treatment with magnetic α-Fe_2O_3/Fe_3O_4 nanoparticles. However, the level of GSH-Px in the cells was significantly decreased by treatment with curcumin, the drug-loaded nanosystem, and the drug-loaded nanosystem assisted with a magnetic field. In addition, the drug-loaded nanosystem with magnetic field assistance had the strongest inhibitory effect on GSH-Px expression in SGC-7901 cells. These results revealed that the drug-loaded nanosystem assisted by a magnetic field could not only reduce the antioxidant capacity of glutathione but also reduced the energy metabolism of SGC-7901 cells, thereby enhancing the level of intracellular free radicals and promoting cell death. However, after the addition of NAC, the level of free radicals in SGC-7901 cells was closer to the steady state, and the expression level of GSH-Px increased. These findings indicated that under a magnetic field condition, the α-Fe_2O_3/Fe_3O_4-CA-CTS-Cur nanosystem exerted a strong ability to inhibit GSH-Px production, which was approximately 3.6 folds lower than that of the control group. Consequently, the structure and function of the cells were no longer intact, prompting the cells to enter the death stage.

ROS were oxygen-containing and active substances produced in the body. ROS was the main medium through which phagocytes played a role in phagocytosis and killing. However, excessive ROS could cause cell damage (Jelic et al., 2021; Xu et al., 2011). Fig. 12D showed the ROS content of SGC-7901 cells stained with DCFH-DA using flow cytometry. As shown in Fig. 12D, the ROS content in SGC-7901 cells was only slightly increased after treatment with magnetic α-Fe_2O_3/Fe_3O_4 nanoparticles, indicating that this nanomaterials had almost no effect on ROS levels in SGC-7901 cells and that their biocompatibility was excellent. ROS content increased greatly in curcumin, drug-loaded nanosystem, and drug-loaded nanosystem assisted by a magnetic field. In particular, the ROS content of the drug-loaded nanosystem under a magnetic field increased nearly twice as much as that of the control group. Reactive oxygen species attacked cells, causing oxidative damage and promoting cell death. Therefore, the most severe damage was observed under the action of the α-Fe_2O_3/Fe_3O_4-CA-CTS-Cur nanosystem assisted with magnetic assistance. In addition, with NAC, the ability of the drug-loaded nanosystem assisted with a magnetic field to promote ROS production in SGC-7901 cells was inhibited, indicating that NAC could remove ROS, which confirmed the mediating effect of the drug-loaded nanosystem assisted by the magnetic field on ROS generation. To further detect the ROS levels under the action of the different test nanomaterials, confocal laser microscopy was used to observe the staining of SGC-7901 cells. As shown in Fig. 12H, Hoechst 33,342 was a blue fluorescent dye that could penetrate the membranes of living cells and interact with genetic nanomaterials. DCFH-DA was a fluorescent dye used for the detection of reactive oxygen species, which could emit green fluorescence only when it was hydrolyzed and oxidized into DCF after entering the cells. As shown in Fig. 12H, magnetic α-Fe_2O_3/Fe_3O_4 nanoparticles produced very little amount of ROS with or without a magnetic field, which might be attributed to an increase in oxidation caused by the release of iron ions from ferrites. However, in the curcumin group, the drug-loaded nanosystem, and drug-loaded nanosystem assisted with a magnetic field, and the green fluorescence in the corresponding figure was significantly enhanced, indicating that these three drugs had a mediating effect on the increase in ROS level. In addition, under the action of a magnetic field, SGC-7901 cells produced the strongest fluorescence with the α-Fe_2O_3/Fe_3O_4-CA-CTS-Cur nanosystem, indicating the maximum ROS content at this time.

Lactate dehydrogenase (LDH) was an important enzyme in glycolysis, and its level was related to cell damage. A high LDH content was associated with severe cell damage (Forkasiewicz et al., 2020). Therefore, the LDH content in the cells treated with α-Fe_2O_3/Fe_3O_4-CA-CTS-Cur nanosystem under a magnetic field was significantly higher than that in the other groups, indicating that the highest intensity of cell damage occurred in this group (Fig. 12E). The LDH content in the magnetic α-Fe_2O_3/Fe_3O_4 nanoparticles group was higher than that in the control group, which was caused by mechanical damage in the washing process. NAC inhibited the production of ROS and reduced oxidative stress and cell damage. Therefore, NAC could reduce cell damage caused by the drug-loaded nanosystem assisted by a magnetic field. Notably, in the magnetic field-assisted group, the content of the drug-loaded nanosystem entering the cells increased significantly due to the targeting effect of magnetic fields, and the loaded curcumin in the drug-loaded nanosystem was hydrolyzed and released in the acidic environment of SGC-7901 cells, causing damage to the cells. Moreover, ferrite in the α-Fe_2O_3/Fe_3O_4-CA-CTS-Cur nanosystem released iron ions, which was conducive to ferroptosis, resulting in intensified oxidative stress and serious cell damage. This result was consistent with the previous findings. In summary, the α-Fe_2O_3/Fe_3O_4-CA-CTS-Cur nanosystem promoted cell damage under a magnetic field, and it had the potential to suppress SGC-7901 cells.

As an antioxidant, NAC, a precursor of reduced glutathione, could increase the scavenging of free radicals in cells and protect them from oxidative stress damage. If the expressions of proteins associated with apoptosis and ferroptosis were significantly influenced by the addition of NAC, the mechanism of the α-Fe_2O_3/Fe_3O_4-CA-CTS-Cur nanosystem assisted by a magnetic field could be further confirmed in the flank direction (Sun et al., 2018). Fig. 12F and S7 showed the results of the western blotting analysis of P53, Bax, Bcl-2, Cyto C, cleaved-caspase 9, and cleaved-caspase 3 of the drug-loaded nanosystem assisted by a magnetic field with or without NAC addition. The expression level of P53 protein was significantly reduced after the addition of NAC. In this case, the activating effect of P53 on the pro-apoptotic protein Bax and the inhibitory effect of the anti-apoptotic protein Bcl-2 was low. Therefore, the lower levels of pro-apoptotic proteins were not conducive to the release of cytochrome *C*. The activation of caspase 9 and caspase 3, two key proteins in the caspase pathway, was reduced. These results indicated that the presence of antioxidant NAC reduced the apoptotic effect of drug-loaded nanosystem on SGC-7901 cells, which confirmed that the α-Fe_2O_3/Fe_3O_4-CA-CTS-Cur nanosystem assisted by a magnetic field could induce apoptosis through the caspase pathway.

Fig. 12G and S8 display the effect of the magnetic field-assisted α-Fe_2O_3/Fe_3O_4-CA-CTS-Cur nanosystem on proteins associated with ferroptosis in SGC-7901 cells with or without NAC involvement. With the addition of NAC, the reduction in FTH1 content caused by the stimulation of the drug-loaded nanosystem was alleviated, indicating that NAC facilitated the maintenance of intracellular iron balance. In addition, GPX4 content was significantly increased under the action of NAC, indicating that NAC reduced the effect of a drug-loaded nanosystem assisted by a magnetic field on the accumulation of peroxide products in SGC-7901 cells. This was consistent with the effects of NAC on MDA, SOD, GSH, and ROS. The addition of NAC could significantly reduce ferroptosis, which was characterized by lipid peroxidation caused by the α-Fe_2O_3/Fe_3O_4-CA-CTS-Cur nanosystem under a magnetic field. Furthermore, we confirmed that a drug-loaded nanosystem with a magnetic field could induce cell death through the ferroptosis pathway.

4. Conclusions

The heterogeneous magnetic α-Fe_2O_3/Fe_3O_4 nanoparticles were successfully prepared via the rapid combustion process, the average particle size and saturation magnetization of the heterogeneous nanoparticles calcined at 400 °C for 2.0 h with the heating rate of 3 °C/min were 24.9 nm and 70.9 emu/g, respectively. Heterogeneous magnetic α-Fe_2O_3/Fe_3O_4 nanoparticles were modified with citric acid and chitosan, and loaded curcumin to successfully construct magnetic α-Fe_2O_3/Fe_3O_4-CA-CTS-Cur nanosystem. The average thickness and size of the magnetic core were 9.5 nm and 25.2 nm, respectively, and the saturation magnetization was 30.3 emu/g.

The α-Fe_2O_3/Fe_3O_4-CA-CTS-Cur nanosystem had stable pH-sensitive drug release capability, effectively enabled curcumin to enter the cells for action, exhibited a robust inhibitory effect on the proliferation, invasion, and migration of SGC-7901 cells, promoted oxidative damage and apoptosis in SGC-7901 cells through caspase and ferroptosis mechanisms, and demonstrated low toxic side effects on normal tissue GES-1 cells.

The successful construction of α-Fe_2O_3/Fe_3O_4-CA-CTS-Cur nanosystem not only provided basic data for vivo research, but also established a model for the delivery of insoluble drugs; owing to their facile entering into cells, it expanded the space of new materials applications in cancer treatment, and also provided a new idea for breaching the blood–brain barrier (BBB) of drug carry. The α-Fe_2O_3/Fe_3O_4-CA-CTS-Cur nanosystem would have a promising prospect in the biomedical field.

CRediT authorship contribution statement

Mingyi Ma: Investigation, Data curation, Methodology, Writing – original draft. **Zhixiang Lv:** Resources, Project administration, Writing – review & editing. **You Li:** Methodology, Writing – original draft, Data curation. **Ziye Zhu:** Investigation, Data curation. **Chen Ling:** Investigation, Data curation. **Dawei He:** Conceptualization, Methodology, Supervision, Writing – review & editing. **Ruijiang Liu:** Conceptualization, Methodology, Formal analysis, Visualization, Writing – review & editing, Supervision, Funding acquisition.

Declaration of Competing Interest

The authors declare that they have no known competing financial interests or personal relationships that could have appeared to influence the work reported in this paper.

Acknowledgments

This work was supported by the Jiangsu Provincial Postgraduate Scientific Practice and Innovation Project (SJCX20_1432).

Appendix A. Supplementary material

Supplementary data to this article can be found online at https://doi.org/10.1016/j.arabjc.2023.105352.

References

AlSalhi, M.S., Devanesan, S., Shanmugam, P., Kim, Y.O., Kwon, J.T., Kim, H.J., 2020. Synthesis and biocompatible role of hierarchical structured carbon nanoplates incorporated α-Fe_2O_3 nanocomposites for biomedical applications with respect to cancer treatment. Saudi. J. Biol. Sci. 27, 588–593. https://doi.org/10.1016/j.sjbs.2019.11.028.

Asnani, A., Shi, X., Farrell, L., Lall, R., Sebag, I.A., Plana, J.C., Gerszten, R.E., Scherrer-Crosbie, M., 2020. Changes in citric acid cycle and nucleoside metabolism are associated with anthracycline cardiotoxicity in patients with breast cancer. J. Cardiovasc. Transl. 13, 349–356. https://doi.org/10.1007/s12265-019-09897-y.

Bian, J., Girotti, J., Fan, Y., Levy, E.S., Zang, N., Sethuraman, V., Kou, P., Zhang, K., Gruenhagen, J., Lin, J., 2022. Fast and versatile analysis of liposome encapsulation efficiency by nanoParticle exclusion chromatography. J. Chromatogr. A 1662,. https://doi.org/10.1016/j.chroma.2021.462688 462688.

Cao, J., Zheng, M.X., Sun, Z.Y., Li, Z.Y., Qi, X.Y., Shen, S., 2022. One-step fabrication of multifunctional PLGA-HMME-DTX@MnO_2 nanoparticles for enhanced chemo-sonodynamic antitumor treatment. Int. J. Nanomed. 17, 2577–2591. https://doi.org/10.2147/IJN.S365570.

Cui, L., Wang, X., Liu, Z.Y., Li, Z.Q., Bai, Z.W., Lin, K., Yang, J., Cui, Y.L., Tian, F., 2023. Metal-organic framework decorated with glycyrrhetinic acid conjugated chitosan as a pH-responsive nanocarrier for targeted drug delivery. Int. J. Biol. Macromol. 240,. https://doi.org/10.1016/j.ijbiomac.2023.124370 124370.

Da Silva, T.B., Dias, E.A., Cardoso, L.M.D.F., Gama, J.F.G., Alves, L.A., Henriques-Pons, A., 2023. Magnetic nanostructures and stem cells for regenerative medicine. Appl. Liver Dis. IJMS 24, 9293. https://doi.org/10.3390/ijms24119293.

Dafeh, S.R., Iranmanesh, P., Salarizadeh, P., 2019. Fabrication, optimization, and characterization of ultra-small superparamagnetic Fe_3O_4 and biocompatible Fe_3O_4@ZnS core/shell magnetic nanoparticles: Ready for biomedicine applications. Mater. Sci. Eng.: C 98, 205–212. https://doi.org/10.1016/j.msec.2018.12.147.

De Barros, H.R., López-Gallego, F., Liz-Marzán, L.M., 2021. Light-driven catalytic regulation of enzymes at the interface with plasmonic nanomaterials. Biochemistry 60, 991–998. https://doi.org/10.1021/acs.biochem.0c00447.

Du, X., Zhang, P.L., Fu, H.X., Ahsan, H.M., Gao, J., Chen, Q.Y., 2019. Smart mitochondrial-targeted cancer therapy: Subcellular distribution, selective $TrxR_2$ inhibition accompany with declined antioxidant capacity. Int. J. Pharmaceut. 555, 346–355. https://doi.org/10.1016/j.ijpharm.2018.11.057.

Eddarai, E.M., El Mouzahim, M., Boussen, R., Bellaouchou, A., Guenbour, A., Zarrouk, A., 2022. Chitosan-kaolinite clay composite as durable coating material for slow release NPK fertilizer. Int. J. Biol. Macromol. 195, 424–432. https://doi.org/10.1016/j.ijbiomac.2021.12.055.

Fazeli, M., Fazeli, F., Nuge, T., Abdoli, O., Moghaddam, S., 2022. Study on the preparation and properties of polyamide/chitosan nanocomposite fabricated by electrospinning method. J. Polym. Environ. 30, 644–652. https://doi.org/10.1007/s10924-021-02229-9.

Feng, Y.S., Sun, C.Y., Yuan, Y.Y., Zhu, Y., Wan, J.Y., Firempong, C.K., Omari-Siaw, E., Xu, Y., Pu, Z.Q., Yu, J.N., Xu, X.M., 2016. Enhanced oral bioavailability and in vivo antioxidant activity of chlorogenic acid via liposomal formulation. Int. J. Pharmaceut. 501, 342–349. https://doi.org/10.1016/j.ijpharm.2016.01.081.

Feng, X., Xue, Y., Gonca, S., Ji, K., Zhang, M., García-García, F.R., Li, Q., Huang, Y., Kamenev, K.V., Chen, X., 2023. Ultrasmall superparamagnetic iron oxide nanoparticles for enhanced tumor penetration. J. Mater. Chem. B 11, 3422–3433. https://doi.org/10.1039/D2TB02630A.

Fiore, A.M., Varvaro, G., Agostinelli, E., Mangone, A., De Giglio, E., Terzano, R., Allegretta, I., Dell'Anna, M.M., Fiore, S., Mastrorilli, P., 2022. Synthesis and use in catalysis of hematite nanoparticles obtained from a polymer supported Fe(III) complex. Eur. J. Inorg. Chem. 2022. https://doi.org/10.1002/ejic.202100943.

Forkasiewicz, A., Dorociak, M., Stach, K., Szelachowski, P., Tabola, R., Augoff, K., 2020. The usefulness of lactate dehydrogenase measurements in current oncological practice. Cell. Mol. Biol. Lett. 25, 35. https://doi.org/10.1186/s11658-020-00228-7.

Foroozandeh, A., Abdouss, M., SalarAmoli, H., Pourmadadi, M., Yazdian, F., 2023. An electrochemical aptasensor based on g-C_3N_4/Fe_3O_4/PANI nanocomposite applying cancer antigen_125 biomarkers detection. Process Biochem. 127, 82–91. https://doi.org/10.1016/j.procbio.2023.02.004.

Gan, Y.H., Zhang, J., Lei, S.L., Yan, M., Xie, W.T., Qi, X.Y., Wang, H.J., Xiao, J.M., Chen, S.Y., Li, S.J., Tian, G., Zhang, G.L., Wu, Z.Y., 2022. Atomically precise multi-domain $GdxFe_{3-x}O_4$ nanoclusters with modulated contrast properties for T2-weighted magnetic resonance imaging of early orthotopic cancer. Chem. Eng. J. 429,. https://doi.org/10.1016/j.cej.2021.132255 132255.

Gupta, J., Quadros, M., Momin, M., 2023. Mesoporous silica nanoparticles: Synthesis and multifaceted functionalization for controlled drug delivery. J. Drug Deliv. Sci. Tec. 81,. https://doi.org/10.1016/j.jddst.2023.104305 104305.

Hong, Y., Shi, H.B., Shu, X., Zhang, Y., Wu, Y.C., 2018. Tunable synthesis of hierarchical superparamagnetic Fe_3O_4 nanospheres by a surfactant-free solvothermal method. J. Supercond. Nov. Magn. 31, 2959–2967. https://doi.org/10.1007/s10948-017-4533-3.

Huang, Z., Wang, H.W., Hong, J.W., Zhao, L.S., 2023. MOF-derived Fe_2O_3@C-coupled Bi2MoO6 heterojunctions for highly efficient Photo-Fenton degradation of tetracycline. J. Mol. Liq. 383,. https://doi.org/10.1016/j.molliq.2023.122157 122157.

Jafari, H., Namazi, H., Mahdavinia, G.R., 2023. pH-sensitive biocompatible chitosan/sepiolite-based cross-linked citric acid magnetic nanocarrier for efficient sunitinib release. Int. J. Biol. Macromol. 242,. https://doi.org/10.1016/j.ijbiomac.2023.124739 124739.

Jelic, M., Mandic, A., Maricic, S., Srdjenovic, B., 2021. Oxidative stress and its role in cancer. J. Cancer Res. Ther. 17, 22. https://doi.org/10.4103/jcrt.JCRT_862_16.

Jin, G.F., Xiao, F.Y., Li, Z.W., Qi, X.Y., Zhao, L., Sun, X.Y., 2020. Design, synthesis, and dual evaluation of quinoline and quinolinium iodide salt derivatives as potential anticancer and antibacterial agents. ChemMedChem 15, 600–609. https://doi.org/10.1002/cmdc.202000002.

Joshi, B., Samuel, E., Kim, Y., Yarin, A.L., Swihart, M.T., Yoon, S.S., 2022. Progress and potential of electrospinning-derived substrate-free and binder-free lithium-ion battery electrodes. Chem. Eng. J. 430,. https://doi.org/10.1016/j.cej.2021.132876 132876.

Kah, G., Chandran, R., Abrahamse, H., 2023. Curcumin a natural phenol and its therapeutic role in cancer and photodynamic therapy: A review. Pharmaceutics 15, 639. https://doi.org/10.3390/pharmaceutics15020639.

Khuyen, H.T., Huong, T.T., Van, N.D., Huong, N.T., Vu, N., Lien, P.T., Nam, P.H., Nghia, V.X., 2023. Synthesis of multifunctional Eu (III) complex doped Fe3O4/Au nanocomposite for dual photo-magnetic hyperthermia and fluorescence bioimaging. Molecules 28, 749. https://doi.org/10.3390/molecules28020749.

Kong, N., Chen, X.Y., Feng, J., Duan, T., Liu, S.P., Sun, X.N., Chen, P., Pan, T., Yan, L.L., Jin, T., Xiang, Y., Gao, Q., Wen, C.Y., Ma, W.R., Liu, W.C., Zhang, M.M., Yang, Z.Y., Wang, W.G., Zhang, R.N., Chen, B., Xie, T., Sui, X.B., Tao, W., 2021. Baicalin induces ferroptosis in bladder cancer cells by downregulating FTH1. Acta Pharma. Sin. B 11, 4045–4054. https://doi.org/10.1016/j.apsb.2021.03.036.

Kuang, W.W., Hu, W.L., Ren, H., Shao, Y.H., Liu, B.Q., 2021. Plant derived coumestrol phytochemical targets human skin carcinoma cells by inducing mitochondrial-mediated apoptosis, cell cycle arrest, inhibition of cell migration and invasion and modulation of m-TOR/PI3K/AKT signalling pathway. Saudi J. Biol. Sci. 28, 2739–2746. https://doi.org/10.1016/j.sjbs.2021.03.043.

Kumar, S., Clair, D.S., 2021. Radioresistance in prostate cancer: Focus on the interplay between NF-κB and SOD. Antioxidants 10, 1925. https://doi.org/10.3390/antiox10121925.

Lan, Y.T., Veisi, H., Ebrahimi, F., Hemmati, S., Karmakar, B., 2023. Chitosan-starch modified Kaolin for immobilizing Au NPs: Investigation of its catalytic performance, antioxidant potential and study against gastrointestinal cancers. Inorg. Chem. Commun. 156,. https://doi.org/10.1016/j.inoche.2023.111136 111136.

Lee, Y.S., Kim, J., Koo, J.H., Kim, T.-H., Kim, D.-H., 2018. Nanomaterials for bioelectronics and integrated medical systems. Korean J. Chem. Eng. 35, 1–11. https://doi.org/10.1007/s11814-017-0236-5.

Li, Z.X., Cai, W., Liu, J.J., Zhou, M.T., Cheng, L., Yu, H., Song, L., Gui, Z., Hu, Y., 2021. One-pot exfoliation and synthesis of hydroxyapatite-functionalized graphene as multifunctional nanomaterials based on electrochemical approach. Compos. Part A-Appl. s. 149,. https://doi.org/10.1016/j.compositesa.2021.106583 106583.

Li, B., Gong, T.T., Xu, N.N., Cui, F.Z., Yuan, B.Y., Yuan, Q.H., Sun, H.Z., Wang, L., Liu, J.H., 2020. Improved stability and photothermal performance of polydopamine-modified Fe3O4 nanocomposites for highly efficient magnetic resonance imaging-guided photothermal therapy. Small 16, 2003969. https://doi.org/10.1002/smll.202003969.

Li, Z.Q., Wan, W.M., Bai, Z.W., Peng, B., Wang, X., Cui, L., Liu, Z.Y., Lin, K., Yang, J., Hao, J., Tian, F., 2023. Construction of pH-responsive nanoplatform from stable magnetic nanoparticles for targeted drug delivery and intracellular imaging. Sensor. Actuat. B-Chem. 375,. https://doi.org/10.1016/j.snb.2022.132869 132869.

Li, C.L., Yang, S.H., Li, R., Gong, S.Y., Huang, M., Sun, Y.Q., Xiong, G.X., Wu, D.P., Ji, M.J., Chen, Y., Gao, C., Yu, Y.Y., 2022. Dual-aptamer-targeted immunomagnetic nanoparticles to accurately explore the correlations between circulating tumor cells and gastric cancer. ACS Appl. Mater. Interfaces 14, 7646–7658. https://doi.org/10.1021/acsami.1c22720.

Li, S., Zhang, L.H., Li, S.H., Zhao, H.Y., Chen, Y.G., 2021. Curcumin suppresses the progression of gastric cancer by regulating circ_0056618/miR-194-5p axis. Open Life Sci. 16, 937–949. https://doi.org/10.1515/biol-2021-0092.

Li, W., Zhou, Y., Yang, J., Li, H.N., Zhang, H.H., Zheng, P., 2017. Curcumin induces apoptotic cell death and protective autophagy in human gastric cancer cells. Oncol. Rep. 37, 3459–3466. https://doi.org/10.3892/or.2017.5637.

Lin, M.H., Zhang, J., Wan, H., Yan, C.Y., Xia, F., 2021. Rationally designed multivalent aptamers targeting cell surface for biomedical applications. ACS Appl. Mater. Interfaces 13, 9369–9389. https://doi.org/10.1021/acsami.0c15644.

Liu, Z.Y., Wang, X., Chen, X.X., Cui, L., Li, Z.Q., Bai, Z.W., Lin, K., Yang, J., Tian, F., 2023. Construction of pH-responsive polydopamine coated magnetic layered hydroxide nanostructure for intracellular drug delivery. Eur. J. Pharm. Biopharm. 182, 12–20. https://doi.org/10.1016/j.ejpb.2022.11.024.

Lu, Y.P., Zhang, R., Liu, S.Y., Zhao, Y., Gao, J., Zhu, L., 2016. ZT-25, a new vacuolar H+-ATPase inhibitor, induces apoptosis and protective autophagy through ROS generation in HepG2 cells. Eur. J. Pharmacol. 771, 130–138. https://doi.org/10.1016/j.ejphar.2015.12.026.

Ma, M.Y., Chen, X., Yue, Y., Wang, J., He, D.W., Liu, R.J., 2023. Immobilization and property of penicillin G acylase on amino functionalized magnetic $Ni_{0.3}Mg_{0.4}Zn_{0.3}Fe_2O_4$ nanoparticles prepared via the rapid combustion process. Front. Bioeng. Biotechnol. 11, 1108820. https://doi.org/10.3389/fbioe.2023.1108820.

Mahmoodabadi, A.N., Kompany, A., Mashreghi, M., 2018. Characterization, antibacterial and cytotoxicity studies of graphene-Fe_3O_4 nanocomposites and Fe_3O_4 nanoparticles synthesized by a facile solvothermal method. Mater. Chem. Phys. 213, 285–294. https://doi.org/10.1016/j.matchemphys.2018.04.033.

Mandal, S., Samanta, P.K., 2021. Electrochemical growth of metallic zinc and its crystallographic study using Rietveld. Mater. Today 43, 3091–3094. https://doi.org/10.1016/j.matpr.2021.01.579.

Manna, S., Seth, A., Gupta, P., Nandi, G., Dutta, R., Jana, S., Jana, S., 2023. Chitosan derivatives as carriers for drug delivery and biomedical applications. ACS Biomater. Sci. Eng. 9, 2181–2202. https://doi.org/10.1021/acsbiomaterials.2c01297.

Mohamed, H.E.A., Afridi, S., Khalil, A.T., Ali, M., Zohra, T., Salman, M., Ikram, A., Shinwari, Z.K., Maaza, M., 2020. Bio-redox potential of Hyphaene thebaica in bio-fabrication of ultrafine maghemite phase iron oxide nanoparticles (Fe2O3 NPs) for therapeutic applications. Mater. Sci. Eng. C 112,. https://doi.org/10.1016/j.msec.2020.110890 110890.

Mou, Y.H., Wang, J., Wu, J.C., He, D., Zhang, C.F., Duan, C.J., Li, B., 2019. Ferroptosis, a new form of cell death: opportunities and challenges in cancer. J. Hematol. Oncol. 12, 34. https://doi.org/10.1186/s13045-019-0720-y.

Nascimento, C., Castro, F., Domingues, M., Lage, A., Alves, E., de Oliveira, R., de Melo, C., Calzavara-Silva, C.E., Sarmento, B., 2023. Reprogramming of tumor-associated macrophages by polyaniline-coated iron oxide nanoparticles applied to treatment of breast cancer. Int. J. Pharmaceut. 636,. https://doi.org/10.1016/j.ijpharm.2023.122866 122866.

Nave, M., Costa, F.J.P., Alves, C.G., Lima-Sousa, R., Melo, B.L., Correia, I.J., De Melo-Diogo, D., 2023. Simple preparation of POxylated nanomaterials for cancer chemo-PDT/PTT. Eur. J. Pharm. Biopharm. 184, 7–15. https://doi.org/10.1016/j.ejpb.2023.01.009.

Nematollahi, E., Pourmadadi, M., Yazdian, F., Fatoorehchi, H., Rashedi, H., Nigjeh, M. N., 2021. Synthesis and characterization of chitosan/polyvinylpyrrolidone coated nanoporous γ-Alumina as a pH-sensitive carrier for controlled release of quercetin. Int. J. Biol. Macromol. 183, 600–613. https://doi.org/10.1016/j.ijbiomac.2021.04.160.

Ni, Y., Deng, P., Yin, R.T., Zhu, Z.Y., Ling, C., Ma, M.Y., Wang, J., Li, S.S., Liu, R.J., 2023. Effect and mechanism of paclitaxel loaded on magnetic Fe3O4@mSiO(2)-NH2-FA nanocomposites to MCF-7 cells. Drug Deliv. 30, 64–82. https://doi.org/10.1080/10717544.2022.2154411.

Parauha, Y.R., Sahu, V., Dhoble, S.J., 2021. Prospective of combustion method for preparation of nanomaterials: A challenge. Mat. Sci. Eng. B-Adv. 267,. https://doi.org/10.1016/j.mseb.2021.115054 115054.

Pei, Z.F., Lei, H.L., Cheng, L., 2023. Bioactive inorganic nanomaterials for cancer theranostics. Chem. Soc. Rev. 52, 2031–2081. https://doi.org/10.1039/D2CS00352J.

Peter, D.N., Pushpakumar, R., Jayaseelan, E., Ananthi, N., 2021. Ordered cubic mesoporous KIT-5 functionalized with g-C_3N_4 nano particles for the complete discoloration and degradation of cationic dye. Mater. Today 47, 739–746. https://doi.org/10.1016/j.matpr.2020.06.162.

Prabhu, K., Lakshminarayanan, M., Mohankumar, G., Ponpandian, N., Viswanathan, C., 2023. Vertically pillared a-Fe_2O_3 nanorods on carbon yarn as a textile-based stable immunosensor electrode for selective electrochemical sensing of interleukin-6 cancer biomarker. Sensor. Actuat. A-Phys. 357,. https://doi.org/10.1016/j.sna.2023.114419 114419.

Ren, G.R., He, Y., Liu, C.Z., Ni, F.F., Luo, X., Shi, J.Y., Song, Y.L., Li, T., Huang, M., Shen, Q., Xie, H.J., 2022. Encapsulation of curcumin in ZEIN-HTCC complexes: Physicochemical characterization, in vitro sustained release behavior and encapsulation mechanism. LWT 155,. https://doi.org/10.1016/j.lwt.2021.112909 112909.

Saeed, M.S., Seyed-Yazdi, J., Hekmatara, S.H., 2020. Surface modification of MWCNT with cluster form of Fe_2O_3/Fe_3O_4 NPs for improving their microwave absorption performance. Chem. Phys. Lett. 756,. https://doi.org/10.1016/j.cplett.2020.137823 137823.

Shirzadi-Ahodashti, M., Mortazavi-Derazkola, S., Ebrahimzadeh, M.A., 2020. Biosynthesis of noble metal nanoparticles using crataegus monogyna leaf extract (CML@X-NPs, X=Ag, Au): Antibacterial and cytotoxic activities against breast and gastric cancer cell lines. Surf. Interfaces 21,. https://doi.org/10.1016/j.surfin.2020.100697 100697.

Sornsumdaeng, K., Seeharaj, P., Prachayawarakorn, J., 2021. Property improvement of biodegradable citric acid-crosslinked rice starch films by calcium oxide. Int. J. Biol. Macromol. 193, 748–757. https://doi.org/10.1016/j.ijbiomac.2021.10.157.

Srivastava, S., Malik, V., Vishnoi, M., 2021. Study on effects of quantum dots in optoelectronics and hydrogen evolution: A review. Mater. Today 45, 5672–5677. https://doi.org/10.1016/j.matpr.2021.02.467.

Suman, Singh, S., Ankita, Kumar, A., Kataria, N., Kumar, S., Kumar, P., Photocatalytic activity of alpha-Fe_2O_3@CeO_2 and CeO_2@alpha-Fe_2O_3 core-shell nanoparticles for degradation of Rose Bengal dye. J. Environ. Chem. Eng. 9, 106266. https://doi.org/10.1016/j.jece.2021.106266.

Sun, Q., Lu, N.-N., Feng, L., 2018. Apigetrin inhibits gastric cancer progression through inducing apoptosis and regulating ROS-modulated STAT3/JAK2 pathway. Biochem. Bioph. Res. Co. 498, 164–170. https://doi.org/10.1016/j.bbrc.2018.02.009.

Tang, L., Zhang, A.N., Zhang, Z.Y., Zhao, Q.Q., Li, J., Mei, Y.J., Yin, Y., Wang, W., 2022. Multifunctional inorganic nanomaterials for cancer photoimmunotherapy. Cancer Commun. 42, 141–163. https://doi.org/10.1002/cac2.12255.

Wang, H.Y., Cheng, Y., Mao, C., Liu, S., Xiao, D.S., Huang, J., Tao, Y.G., 2021. Emerging mechanisms and targeted therapy of ferroptosis in cancer. Mol. Ther. 29, 2185–2208. https://doi.org/10.1016/j.ymthe.2021.03.022.

Wang, Y.K., Chiang, W.C., Kuo, F.C., Wu, M.C., Shih, H.Y., Wang, S.S.W., Liu, C.J., Chen, Y.H., Wu, D.C., Su, W.W., Huang, Y.L., 2018. Levels of malondialdehyde in the gastric juice: Its association with Helicobacter pylori infection and stomach diseases. Helicobacter 23, e12460.

Wang, X.Y., Cui, X.J., Zhao, Y.L., Chen, C.Y., 2020. Nano-bio interactions: the implication of size-dependent biological effects of nanomaterials. Sci. China Life Sci. 63, 1168–1182. https://doi.org/10.1007/s11427-020-1725-0.

Wang, Q., Du, X., Zhou, B.J., Li, J., Lu, W.L., Chen, Q.Y., Gao, J., 2017. Mitochondrial dysfunction is responsible for fatty acid synthase inhibition-induced apoptosis in breast cancer cells by PdpaMn. Biomed. Pharmacother. 96, 396–403. https://doi.org/10.1016/j.biopha.2017.10.008.

Wang, Y.P., El-Kott, A.F., El-Kenawy, A.E., Xue, L.J., 2021. Decorated CuO nanoparticles over chitosan-functionalized magnetic nanoparticles: Investigation of its anti-colon carcinoma and anti-gastric cancer effects. Arab. J. Chem. 14,. https://doi.org/10.1016/j.arabjc.2021.103201 103201.

Wang, P., Kankala, R.K., Chen, B.Q., Zhang, Y., Zhu, M.Z., Li, X.M., Long, R.M., Yang, D. Y., Krastev, R., Wang, S.B., Xiong, X., Liu, Y.G., 2021. Cancer cytomembrane-cloaked prussian blue nanoparticles enhance the efficacy of mild-temperature photothermal therapy by disrupting mitochondrial functions of cancer cells. ACS Appl. Mater. Interfaces 13, 37563–37577. https://doi.org/10.1021/acsami.1c11138.

Wang, M.Q., Liang, Y., Jiang, X.F., Shen, J., 2023. alpha-Fe_2O_3@Au-PEG-Ce6-Gd nanoparticles as acidic H_2O_2-driven oxygenators for multimodal imaging and synergistic tumor therapy. Langmuir 39, 5333–5341. https://doi.org/10.1021/acs.langmuir.2c03388.

Wang, X., Wang, Y.Y., Xue, Z.F., Wan, W.M., Li, Y.X., Qin, H.L., Zhu, Y., Tian, F., Yang, J., 2023. Magnetic liposome as a dual-targeting delivery system for idiopathic pulmonary fibrosis treatment. J. Colloid. Interf. Sci. 636, 388–400. https://doi.org/10.1016/j.jcis.2023.01.007.

Xu, J.J., Dai, X.M., Liu, H.L., Guo, W.J., Gao, J., Wang, C.H., Li, W.B., Yao, Q.Z., 2011. A novel 7-azaisoindigo derivative-induced cancer cell apoptosis and mitochondrial dysfunction mediated by oxidative stress. J. Appl. Toxicol. 31, 164–172. https://doi.org/10.1002/jat.1577.

Yang, H., Gu, Q.Y., Gao, T.T., Wang, X.B., Chue, P.W., Wu, Q.A., Jia, X.B., 2014. Flavonols and derivatives of gallic acid from young leaves of Toona sinensis (A. Juss.) Roemer and evaluation of their anti-oxidant capacity by chemical methods. Pharmacogn. Mag. 10, 185–190. https://doi.org/10.4103/0973-1296.131034.

Zer, N.S., Ben-Ghedalia-Peled, N., Gheber, L.A., Vago, R., 2023. CD44 in bone metastasis development: A key player in the fate decisions of the invading cells? Clin. Exp. Metastas. 40, 125–135. https://doi.org/10.1007/s10585-023-10203-z.

Zhan, W.H., Li, H.R., Zhou, Y., Li, K., Liu, C.H., In Vivo Imaging Guided GMBP1 Modified Nanoplatform for Real Time Monitoring and Photothermal Therapy of Multidrug Resistance in Gastric Cancer. J. Biomed. Nanotechnol. 19, 963-977. https://doi.org/10.1166/jbn.2023.3599.

Zhang, Y.L., Ouyang, H.Z., Zhang, S.S., Ni, Y., Zhu, Z.Y., Ling, C., He, A.L., Liu, R.J., 2023. Label-free electrochemical bioplatform based on Au-modified magnetic Fe_3O_4/α-Fe_2O_3 hetero-nanorods for sensitive quantification of ovarian cancer tumor marker. Microchem. J. 189,. https://doi.org/10.1016/j.microc.2023.108546 108546.

Zhang, B., Tang, W.S., Ding, S.N., 2023. Magnetic quantum dots barcodes using Fe_3O_4/TiO_2 with weak spectral absorption in the visible region for high-sensitivity multiplex detection of tumor markers. Biosens. Bioelectron. 227,. https://doi.org/10.1016/j.bios.2023.115153 115153.

Zhang, M.L., Wu, H.T., Chen, W.J., Xu, Y., Ye, Q.Q., Shen, J.X., Liu, J., 2020. Involvement of glutathione peroxidases in the occurrence and development of breast cancers. J. Transl. Med. 18, 247. https://doi.org/10.1186/s12967-020-02420-x.

Zhang, H.Y., Zhu, Y., Sun, C.Y., Xie, Y.J., Adu-Frimpong, M., Deng, W.W., Yu, J.N., Xu, X. M., Han, Z.F., Qi, G., 2020. GSH responsive nanomedicines self-assembled from small molecule prodrug alleviate the toxicity of cardiac glycosides as potent cancer drugs. Int. J. Pharmaceut. 575,. https://doi.org/10.1016/j.ijpharm.2019.118980 118980.

Zhao, J., Long, X.H., Li, Z.H., Tu, Y.J., 2021. Detection of 2,4-Dinitrophenol and Bio-Imaging Application with Agaric-Based Nitrogen-Doped Carbon Quantum Dots (N-CQDs). J. Braz. Chem. Soc. https://doi.org/10.21577/0103-5053.20210110.

Zhu, L.J., Chen, D.Z., Zhu, Y., Pan, T.T., Xia, D.C., Cai, T.C., Lin, H.W., Lin, J., Jin, X.Z., Wu, F.L., Yu, S.J., Zhu, K.L., Xu, L.M., Chen, Y.P., 2021. GPX4-regulated ferroptosis mediates S100-induced experimental autoimmune hepatitis associated with the Nrf_2/HO^{-1} signaling pathway. Oxid. Med. Cell. Longev. 2021, 1–16. https://doi.org/10.1155/2021/6551069.

Zhu, X.D., Li, S.L., 2023. Nanomaterials in tumor immunotherapy: new strategies and challenges. Mol. Cancer 22, 94. https://doi.org/10.1186/s12943-023-01797-9.

Zou, Y.Y., Chai, Q.L., Zhu, T., Yu, X.X., Mao, G.B., Li, N.X., Chen, J.Y., Lai, G.S., 2022. Simultaneously colorimetric detection and effective removal of mercury ion based on facile preparation of novel and green enzyme mimic. Spectrochim. Acta A 266,. https://doi.org/10.1016/j.saa.2021.120410 120410.